NTNU – Trondheim
Norwegian University of
Science and Technology

Lifetime degradation in n-type Cz-Si

Vivian Sporstøl Koien

Materials Technology
Submission date: June 2012
Supervisor: Eivind Øvrelid, IMTE
Co-supervisor: Mari Juel, SINTEF

Norwegian University of Science and Technology
Department of Materials Science and Engineering

Preface

This work on investigating the effect of donors, thermal donors and defects on the lifetime of an n-type Cz ingot is done as my masters theses, finishing off my education as a sivil engeneer in material science at NTNU, the Norwegian University of Science and Technology. It was carried out between 15th of January and 15th of June in the spring of 2011, in cooperation with SINTEF Materials and Chemistry.

My supervisors were Eivind Øvrelid, associate professor II at NTNU, and Mari Juel, researcher at SINTEF. Thank you both for giving me great guidance in the lab, and with writing this report. I also want to show appreciation for providing me with such an interesting assignment. A special thanks to Yu Hu, PhD student at NTNU, for providing me with training in lifetime measurements, assisting with the Cupper decoration process at NTNU Nanolab, help with inerpretating defect patterns and CDI. Lastly I want to thank Song Zhang, PhD student at NTNU for helping me with the surface passivation and CDI.

Summary

The main object was to investigate the effect of donors, thermal donors and defects on the lifetime on n-type Czochralsky (Cz) silicon. Cz is a technique for making monocrystals by dipping a monocrystalline seed into the melt, and pulling the ingot up as the melt solidifies. Samples were prepared by sawing, grinding and polishing. Copper decoration and preferential etching was done to reveal the defects. Resistivity measurements were performed to investigate the donor distribution. The lifetime and oxygen concentration was measured.

The lifetime may be influenced by donors and traps. Traps may be metallic or non-metallic. Dopants and metal contaminants are usually Scheil distributed, which typically involves a relatively stable distribution in most part of the ingot, and a rapid increase in concentration close to the bottom. Metal contaminants may be introduced from the feedstock, and dopants (either n or p dopants) are added to the melt.

Oxygen is dissolved from the crucible. The oxygen concentration typically decreases with increasing length, and is controlled by the rotation speed. This was confirmed by the interstitial oxygen measurements. The oxygen concentration showed no change after heat treatment, but the presence of oxygen in itself may contribute to produce lifetime reducing agents, such as precipitates and thermal donors.

Thermal donors were found in the first 18cm of the ingot. Both the resistivity and lifetime measurements was used to calculate estimated lifetimes and donor concentrations, respectively. This estimated values were compared with the measured ones, revealing that the lifetime in the ingot was SRH dominated. Thermal donors were found to have less influence on the lifetime than the trapping.

Oxygen precipitations may explain the low lifetime found in the center of the ingot up to about 30cm from the crown. Such precipitations are often gathered in defect bands in the sample. CDI of a Cu decorated sample revealed a pattern of different defect densities, which also showed up at the surface of the sample

after preferential etching. An H- or L- band was believed to be situated here, which both consist of small oxygen precipitates. Defects arize as a funktion of the pulling parameters, and a low growth rate was connected to the low lifetime here.

Indications of the presence of non-metallic traps were found throughout the ingot. However, oxygen precipitates could not explain the non-metallic traps that was found on the outside of the ingot, and the cause of these is therefore unknown. It is however likely that these traps may be connected to the pull-rate/temperature gradient-ratio. Most likely metallic traps were also present. It is uncertain whether the non-metallic or metallic traps were the most important to the lifetime of this ingot, as the relative distribution of the two cannot be decided with certainty from the results in this thesis.

Contrasts in CDI and steep curves using PCD measurements vs length plots were believed to be due to the lifetime degrading agent that changes the fastest. Metallic traps and the phosphorous dopant are known to be Scheil distributed, hence they appear transparent for the lifetime measurements in areas where the distribution is stable. Thermal donors and non-metallic traps are thus more likely to create contrast in the top parts of an ingot. However, it is not necessarily the phenomenon that causes the contrast that is the major lifetime degradation contributor.

Symbols

a - Correction factor (Resistivity calculation)

C_{Ie} - Equilibrium vacancy concentration

C_l - Concentration in the liquid phase

C_n - Auger recombinatin coefficient for electrons

C_p - Auger recombinatin coefficient for holes

C_{0s} - Initial concentration in the solid phase

C_s - Initial concentration in the solid phase

C_{Ve} - Equilibrium interstitial defect concentration

C_{Vs} - Concentration of vacancies before agglomeration

D_I - Diffusivity of interstitial defects

D_V - Diffusivity of vacancies

E - Energy (Orbital levels)

E - Energy of formation

E_c - Energy of the CB

E_f - Energy of the Fermi level

E_g - Band gap

E_i - Ionization energy

E_T - Trap level in band gap

E_v - Energy of the VB

f_s - Fraction of solid phase

$f(x)$ - Calculated resistivity (Standard deviation)

G - Generation rate (excitation)

G - Temperature gradient (Cz pulling)

I - Current

k_B - Boltzmann constant

k - Constant that describes the relationship between the concentration in the liquid and solid face for an impurity

m_0 Electronic rest mass $= 9.10938188 * 10^{31}$kg

m_{th} Thermal electronic mass

n - Total concentration of electrons

n_0 - Dopant density (see N_D)

Δn - Excess electron concentration

N_D - Dopant density (see n_0)

n_D - Total donor density, including thermal donors

n_i - Intrinsic electron concentration

$n_{parameters}$ - Number of parameters (Standard deviation)

n_{points} - Amount of points measured (Standard deviation)

N_T - Trap density

p - Total concentration of holes

p_0 - Concentration of holes due to doping

Δp - Excess hole concentration

p_0 - Concentration of holes due to doping

R - Radius

q - Electronic charge

s - Probe spacing

s - Standard deviation

t - Thickness (sample)

t - Time

T - Temperature

T_m - Melting temperature

T_n - $\frac{T}{300}$

T_nuc - Vacancy nucleation temperature

U - Recombination rate

V - Voltage

V - Growth rate (Cz)

W_p - Watt peak

Y - Length (distance from the shoulder of the ingot)

X - Concentration of non-metallic traps

y_i - Measured resistivity (standard deviation)

ε_I - Drift energy interstitials

ε_V - Drift energy vacancies

ρ - Resistivity

μ - Mobility

μ_n - Mobility of electrons

μ_p - Mobility of holes

σ - Conductivity

σ_n - Capture cross section, electrons

σ_p - Capture cross section, holes

τ - Lifetime

τ_{Auger} - Lifetime for Auger recombination

τ_b - Bulk lifetime

τ_{eff} - Effective lifetime

τ_n - Lifetime of electrones

τ_p - Lifetime of holes

τ_r - Lifetime

τ_{rad} - Lifetime for radiative recombination

τ_s - Surface lifetime

τ_{SRH} - Lifetime for SRH recombination

υ_{th} - Thermal velocity

Contents

Preface i

Summary iii

Symbols v

Contents ix

Introduction 1

1 Theory 3

1.1 Lifetime 4

1.2 Producing Si monocrystals 6

1.2.1 The furnace 6

1.2.2 Growing the ingot 7

1.3 Dopants and other impurities 10

1.3.1 Impurity distribution in the ingot 10

1.3.2 Thermal donors 11

1.3.3 Impurity effects on lifetime 13

1.4 Crystal defects 15

1.4.1 Self interstitials and vacancies 15
1.4.2 Oxygen particles 17
1.5 Characterization methods 19
1.5.1 Cu-decoration 19
1.5.2 Oxygen concentration measurements 19
1.5.3 Resistivity measurements 20
1.5.4 Lifetime measurements with PCD 20
1.5.5 Lifetime measurements with CDI 21

2 Experimental **23**
2.1 The samples 24
2.2 Cu-decoration and etching 26
2.3 Oxygen measurements 27
2.4 Resistivity measurements 27
2.5 Lifetime measurements 27
2.5.1 PCD 27
2.5.2 CDI 28

3 Results **29**
3.1 Cu-decoration and etching 30
3.1.1 Microscopy images, sample 3 32
3.1.2 Microscopy images, sample 4 34
3.1.3 CDI, sample 4 35
3.2 Oxygen concentration 38
3.3 Resistivity 40
3.4 Lifetime 43

4 Discussion **45**

4.1 Etch defects 46

4.2 Oxygen distribution 50

4.3 Resistivity measurements 52

4.4 Lifetime measurements 57

4.5 Doping and impurity effects 59

4.5.1 Dopant and thermal donor calculations 59

4.5.2 Lifetime estimations assuming Auger recombination . . . 67

4.5.3 Lifetime estimations assuming SRH recombination 70

4.5.3.1 Example with iron traps 71

4.5.3.2 The cause of non-metallic traps 81

4.6 Contributions to lifetime degradation in CZ2 85

4.7 Contrast in lifetime measurements 89

Conclusion **91**

Further work **93**

References **93**

Bibliography **93**

Appendices **100**

Appendix 1 100

Appendix 2 101

Appendix 3 103

Appendix 4 105

Appendix 5 107

Introduction

The main motivation for making solar cells is to preserve the environment. Silicon is relatively cheap and non-toxic, (1; 2), and therefore a good choice of material. Silicon solar cells also produce far less CO_2 pr. unit of energy compared to fossil products, even when the production emissions are considered. Another benefit is that silicon is the traditional solar cell material, and a lot of research has already been done on it. The main drawback is that today's solar cells are not commercially competitive with the current commercial energy sources (3).

Figure 0.0.1: Solar panels (4)

The solar cells are made from thin wafers that are sawed out from ingots. To produce the p-n junction, which forces the current to move uni-directionally through the cell, the wafer is differently doped on each side. The most common way of doing this is to make the ingot p-type, and diffuse a thin layer of the n-dopant directly into the finished wafer, so that it is in surplus here. (5). However, in the last few years, n-type ingots have received increased attention, as they don't suffer from illumination degradation, as p-type silicon does(6). After the doping process, the wafers are sent through a series of treatments

to attach the electrodes, protect the material and increase the efficiency of the cells. Lastly, they are assembled on a panel and interconnected, as illustrated in figure 0.0.1.

The most important factor for the commercialization of solar cells is the price pr. Watt peak ($\frac{€}{W_p}$). Multicrystalline solar cells have relatively low costs, but the efficiency of the cells is at the same time reduced due to crystal defects related to the grain boundaries (7; 8). Monocrystalline solar cells balance the ($\frac{€}{W_p}$) relationship differently, as they are more expensive, but the efficiency is also much better. Though improvements to the efficiency can be made through various approaches, such as the treatment technology of the wafers or by the use of mirrors, this work will focus on the material itself. Characterization of an n-type monocrystalline ingot was done using the methods explained in section 1.5. The Czochralsky (Cz) method, which is the dominant commercial method for producing monocrystals (9), is explained in section 1.2.

Lifetime a measure of how long an electron stays excited before it recombines, which is further explained in section 1.1. Having a high lifetime is crucial for making high efficiency solar cells (10). In Cz ingots, the lifetime usually decreases with length (5). There are several factors that are known to influence the lifetime in mono-Si, and the goal is to investigate the influence of each of these.

N-dopants like phosphorous decrease the lifetime, and impurities like iron create effective traps. The concentration of impurities usually increase with increasing length of the ingot, which is further explained further in section 1.3.1. *Thermal* donors is a temperature dependent effect of oxygen contamination, which influence the lifetime similarly to normal donors, and is explained in section 1.3.2. The lifetime is also affected the amount an efficiency of traps in the ingot. The traps may be caused by contaminants or different types of disruptions in the lattice structure. Different types of defects are typically distributed into separate sections of the ingot, which is further explained in section 1.4.

In the experimental part in chapter 2, the lifetime was measured on different parts of the n-type ingot CZ2, using both a photoconductive decay instrument (PCD) and carrier density imaging (CDI). Resistivity measurements were taken and used to calculate the donor distribution in the ingot. This was done both before and after heat treatment to investigate the effect of potential thermal donors. The donor levels were then used to calculate the estimated lifetimes for the ingot. Copper decoration and preferential etching was performed to reveal the defects in the crystal structure. The interstitial oxygen concentration was measured. The measurement results were presented in chapter 3. Calculations and discussions were presented in chapter 4.

Chapter 1

Theory

1.1 Lifetime

Lifetime τ is a measure of how long an electron in a semiconductor stays exited before it recombines with a hole. The lifetime for electrons can be described by equation 1.1, and by equation 1.2 for holes (11). Δn denotes the excess electron carriers, Δp the excess hole carriers and U is the recombination rate. The equilibrium carrier density is denoted n_0 for electrons and p_0 for holes, and the total carrier density is given by $n = n_0 + \Delta n$ for electrons and $p = p_0 + \Delta p$ for holes. For steady state, the generation rate G is equal to U.

$$\tau = \frac{\Delta n}{U} \tag{1.1}$$

$$\tau = \frac{\Delta p}{U} \tag{1.2}$$

An electron can be recombined with a hole through three possible mechanisms: radiative recombination, Auger recombination and Shockley-Read-Hall (SRH) recombination (12). The total lifetime τ of a material is related to the individual lifetimes of these three mechanisms as shown in equation 1.3. τ_{SRH} characterizes the time in excitation before SRH-recombination happens, τ_{rad} of radiative, and τ_{Aug} of Auger recombination.

$$\tau = \frac{1}{\tau_{rad}^{-1} + \tau_{Aug}^{-1} + \tau_{SRH}^{-1}} \tag{1.3}$$

Radiative recombination is when an electron in the conduction band relaxes by emitting a photon with energy of the same size the band gap (12), but is uncommon in silicon. Auger recombination is when the electron instead donates it's energy to a second electron in the conduction band or a hole in the valence band, as illustrated in figure 1.1.1. The second electron (or hole) then relaxes by emitting phonons.

SRH recombination, illustrated in figure 1.1.2, is when the electron get's trapped by an energy level within the band gap. These levels are introduced by impurities (or surface states), and are often referred to as trapping levels. Electrons that are trapped must relax a second time to fully recombine with a hole in the valence band. Oxygen introduces a trap level about 0.17eV below the conduction band when it's trapped by a vacancy (13). However, the most effective traps are those closer to the middle of the band gap. A typical example of this is iron, which introduces a trap level of around $E_V + 0.38eV$ (14).

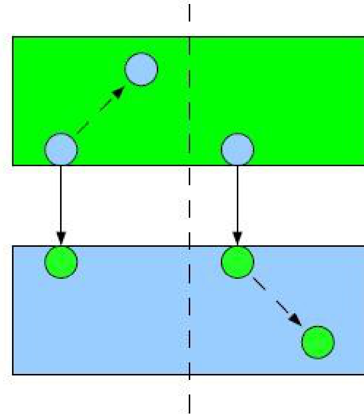

Figure 1.1.1: Auger recombination. The green rectangle represents the conduction band, the blue rectangle the is valence band. The left side of the dotted line illustrates the case where the relaxing electron donates its energy to an electron in the conduction band. On the left side the receiver is instead a hole in the valence band. Both cases are possible.

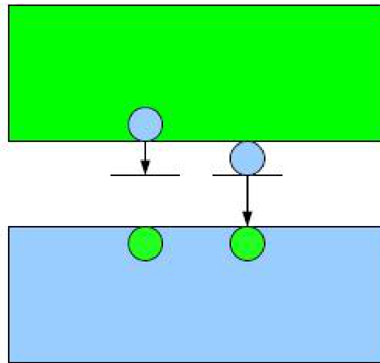

Figure 1.1.2: Shockley-Read-Hall (SRH) recombination. The green rectangle represents the conduction band, the blue rectangle is the valence band. Impurities introduce trap levels in the band gap, forcing the electron to relax in two steps before it can recombine with a hole in the valence band.

1.2 Producing Si monocrystals

The Czochralsky (Cz) method of growing monocrystals was invented by the polish scientist Jan Czochralsky in 1918 (9). It was improved by Teal and Little in the 50s, in total making out the most significant parts of the technology used today (15; 16; 17). Though there exists two methods of producing monocrystals, the Cz and the float zone (Fz) method, the Cz method is heavily dominating on the commercial market today (9).

1.2.1 The furnace

The Czochralsky furnace consists of a lifting- and rotating system, a growth chamber, a hot zone, a vacuum system, and a chamber for receiving the finished crystal (9). Figure 1.2.1 illustrates a typical Cz furnace. A heating system surrounds the crucible to melt and control the temperature of the silicon after the pulling. Underneath the crucible, a spill tray is placed in case the crucible ruptures. A heat shield around the structure prevents the heat from escaping the hot zone, the structural part of the furnace that keep the temperature at appropriate levels around the crystal and the melt.

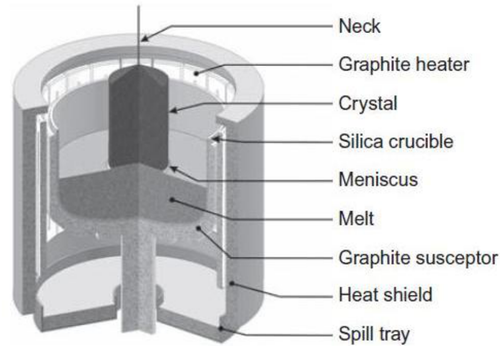

Figure 1.2.1: The structure of a Czochralsky furnace (9).

The melt is contained in a silica crucible, and the cylindrical monocrystal is pulled out of the melt and into the receiving chamber (9). This all happens in an inert atmosphere, to prevent contamination of the melt, most commonly argon gas at low pressure. The inert gas also blows away $SiO_{(g)}$ that evaporates from the melt, preventing it gas to react with the liquid surface and end up in the ingot, as oxygen is dissolved into the melt from the silica crucible. Figure

1.2.2 illustrates the gas flow and how oxygen dissolves and evaporates from the melt.

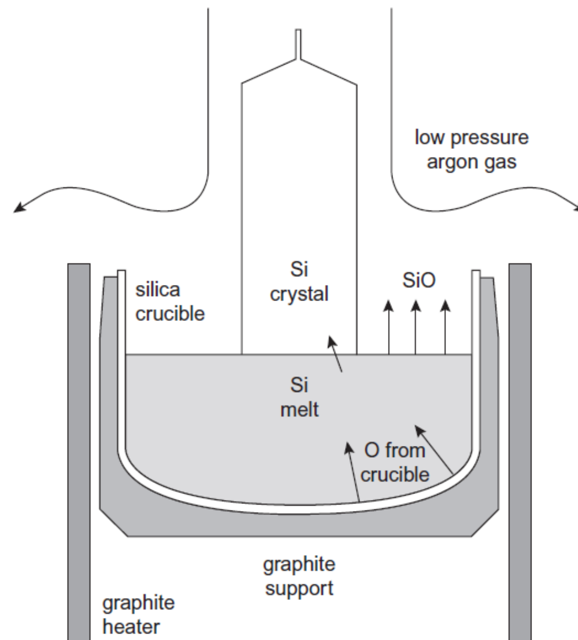

Figure 1.2.2: Oxygen is dissolved from the silica crucible, and can evaporate as $SiO_{(g)}$. To prevent the SiO from reacting with the melt again, it is blown away by an inert gas, typically argon.

There are very few alternative materials that is suited for use in the crucible (9). Almost all elements are considered too reactive to satisfy the purity requirements of the melt. Metals, group III and IV-elements, ceramics, nitrogen, carbon are all harmful choices for the material. Thus, the crucible is usually made of high-purity silica, as oxygen is a pollutant of "lesser evil". Only 1-2 % of the dissolved oxygen ends up in the ingot.

1.2.2 Growing the ingot

The first step is to charge the crucible with polycrystalline silicon pieces of different sizes (9). A very pure feedstock is necessary to get the quality of the ingot to be as high as possible. The dopants are added as solid alloys to enhance the mixing abilities of the dopants with the melt, as they otherwise can be hard to distribute evenly. The temperature inside the hot zone is brought to approximately 1500°C and maintained there to fully melt the feedstock. The melting

point of silicon is 1410ºC (18). After melt down, the temperature is stabilized to a preferred temperature above the melting point based on experience from previous growths (9).

The next step is the dipping of the seed (9). A small part of it will melt and produce a meniscus, i.a. the solidification front, and if the conditions in the furnace are right, the liquid around the seed will start to solidify onto it with the same orientation as the seed. As it grows, the crystal will be pulled up from the melt. At first the growing crystal will be pulled relatively fast so that it grows only in length, and not in width, producing the neck. The reason for the necking step is to get rid of dislocations that may appear because of the thermal shock the seed experiences before the interface between the solid and the liquid phase is stable. Figure 1.2.3 illustrates the ingot during the pulling process (19). The liquid is glowing of yellow in this picture.

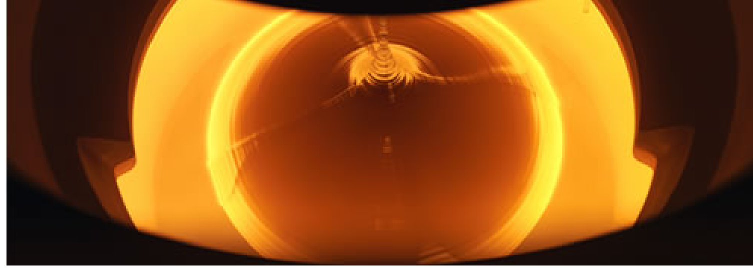

Figure 1.2.3: The first step is to grow the neck, which is the thin cylindrical part above the crown of the ingot. The neck is made to ensure that no dislocations are growing into the body. The crown is where the ingot starts to flatten, and the body of the ingot is the cylindrical part below the crown (19).

The thin neck forces these dislocations to grow out of the crystal, utilizing the fact that they move faster in certain crystal directions than other (9). The crystal orientation of the seed is therefore very important, and most commonly it's grown from the {100} plane. Dislocations grow the fastest in the <110> direction, making them grow out of the solid because of the angle.

Once the neck is complete, the pulling speed and temperature are lowered so that the crystal can grow in width and produce the crown of the ingot (9). The conditions in the crown set the standards for the conditions in the body . A flat crown means that less material is wasted, but a sloping crown makes the transition to the body easier. The diameter of the ingot is monitored by a camera, and the temperature and pulling speed is regulated based on this information.

When the desired crown diameter is achieved, the temperature is further lowered and the pulling rate increased, so that the crystal only grows in length again

(9). This part is what makes out the body of the ingot, and is where the wafers are cut from. The cylindrical shape is due to the opposite rotation of the ingot versus the crucible, and a magnetic field is often applied to stabilize the melt from convection. The temperature of the gas flow also has some impact on the shape of the ingot.

After the body is finished, a tail is produced to reduce the impact of a new thermal shock (9). The tail is the part where the ingot starts narrowing again. The steeper the tail is, the less thermal shock the ingot has to endure, reducing the number of dislocations caused by this. A second benefit is that the dislocations impose less damage to the body, and more to the tail itself. Figure 1.2.4 shows two finished Czochralsky silicon ingots (19). Maximum crystal weights are several hundreds of kg, though all commercial crystal sizes can be made (9).

Figure 1.2.4: Two complete Czochralsky monocrystalline ingots with the crown on the right hand side, and the tail on the left (19).

1.3 Dopants and other impurities

1.3.1 Impurity distribution in the ingot

Impurities in silicon can be classified into two categories: dopants and contaminants (20). In the Cz process, dopants and impurities like phosphorous and iron are distributed in the ingot according to Scheil's equation, shown in equation 1.4 (21). The equation assumes complete mixing in the melt, and no diffusion in the solid. C_s is the concentration in the solid phase, C_{0s} is the *initial* concentration in the solid phase, f_s is the fraction of solid, and k is a constant described by equation 1.5.

$$\frac{C_s}{C_{s0}} = (1 - f_s)^{k-1} \tag{1.4}$$

$$k = \frac{C_s}{C_l} \tag{1.5}$$

For phosphor, k is equal to 0.35. Iron is a common polluting impurity that has a k-value of $1.5 * 10^{-6}$(22). Figure 1.3.1 shows a typical distribution of impurities in an ingot.

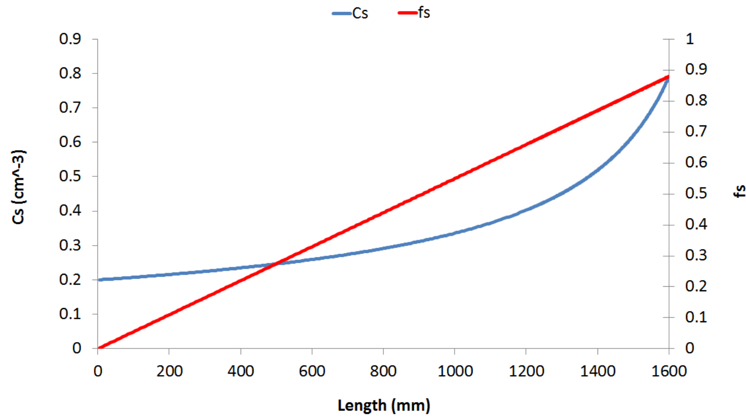

Figure 1.3.1: A typical distribution of impurities in an ingot. The impurities congest to the liquid phase, causing an exponential increase in concentration towards the bottom of the ingot.

The impurities are congesting to the liquid phase due to the solubility in the liquid phase being greater than the solid phase (21). This is the reason for the

exponential shape of the curve with increasing the length, and the quality of the wafers are thus depending on where in the ingot they are cut from.

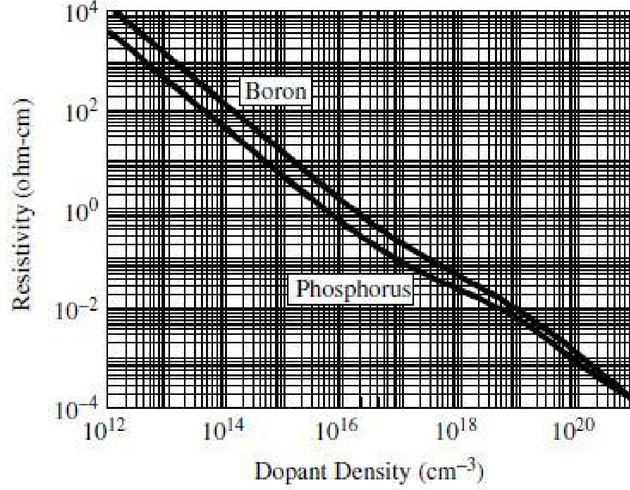

Figure 1.3.2: The relationship between the resistivity and the dopant concentration.

Figure1.3.2 shows the relationship between the phosphorous concentration (or boron for p-type Si) and the resistivity ρ (11). The dopant concentration n_D can be calculated from the resistivity as shown in equation 1.6 (23). Z is described by equation 1.7.

$$n_D = \frac{6.242 * 10^{18}}{\rho} * 10^Z \tag{1.6}$$

$$Z = \frac{A_0 + A_1 x + A_2 x^2 + A_3 x^3}{1 + B_1 x + B_2 x^2 + B_3 x^3} \tag{1.7}$$

$x = log\ \rho$, $A_0 = -3.1083$, $A_1 = -3.2626$, $A_2 = -1.2196$, $A_3 = -0.13923$, $B_1 = 1.0265$, $B_2 = 0.38755$ and $B_3 = 0.041833$.

1.3.2 Thermal donors

Oxygen is dissolved from the crucible, and is controlled by the rotation rate. Correspondingly, the oxygen concentration does *not* follow Scheil's equation.

Having the same crucible rotation rate throughout the pull, the oxygen concentration is expected to *decrease* (5; 24). Figure 1.3.3 shows an example of the oxygen distribution in two different ingots from O'Mara (24).

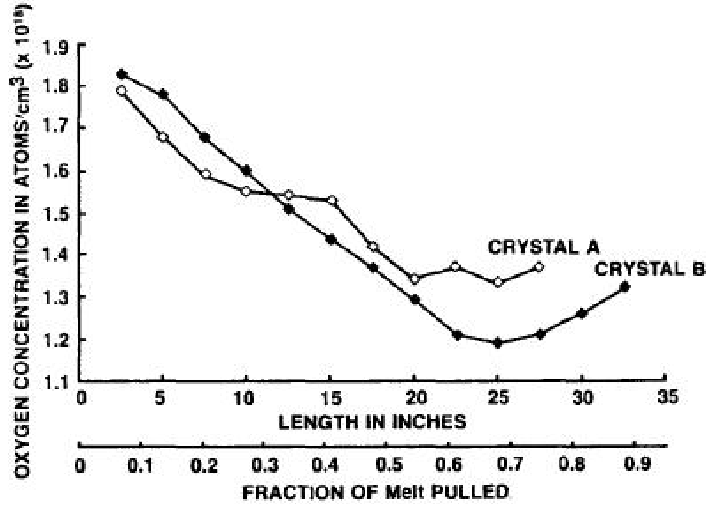

Figure 1.3.3: A typical decreasing distribution of oxygen in an ingot, shown by two examples from O'Mara (24)

Thermal donors is an effect of interstitial oxygen being present in silicon that has been annealed to between 350-500 ºC (25; 13). Oxygen then donates 2 electrons to the lattice, in other word it becomes an n-type double donor. Thermal donors can be removed by annealing to above 500 ºC.

According to Veirman et. al., thermal donors can be mapped by measuring the resistivity before and after thermal donor killing (26). The general relationship between the resistivity and the donor concentration N is shown in equation 1.8, where q is the electronic charge= $1.60217646 * 10^{-19}$ C. The mobility µ(N) can be calculated by equation 1.9 (27), where T is the temperature in Kelvin, and $T_n = \frac{T}{300}$.

$$\rho = \frac{1}{N * q * \mu(\text{N})} \tag{1.8}$$

$$\mu(N) = 88T_n^{-0.57} + \frac{7.4 * 10^8 * T^{-2.33}}{1 + \frac{N}{1.26*10^{17}*T_n^{2.4}} * 0.88 * T_n^{-0.146}} \tag{1.9}$$

For samples with no thermal donors, N is equal to the dopant density N_D, as shown in equation 1.10(26). The mobility can then be described by equation 1.11. However, if thermal donors *are* present, N is described by $N = N_D + 2[TD]$ for n-type Si with electron densities $n < 5 * 10^{15}$. The concentration of thermal donors [TD] is multiplied with a factor of 2, due to the double donor effect. The resistivity with thermal donors being present is described by equation 1.12, and correspondingly the mobility is described by equation 1.13.

$$\rho_1 = \frac{1}{N_D * q * \mu(N_D)} \tag{1.10}$$

$$\mu(N_D) = 88T_n^{-0.57} + \frac{7.4 * 10^8 * T^{-2.33}}{1 + \frac{N_D}{1.26*10^{17}*T_n^{2.4}} * 0.88 * T_n^{-0.146}} \tag{1.11}$$

$$\rho_2 = \frac{1}{(N_D + 2[TD]) * q * \mu(N_D + 2[\mathrm{TD}])} \tag{1.12}$$

$$\mu(N_D + 2[TD]) = 88T_n^{-0.57} + \frac{7.4 * 10^8 * T^{-2.33}}{1 + \frac{N_D+2[TD]}{1.26*10^{17}*T_n^{2.4}} * 0.88 * T_n^{-0.146}} \tag{1.13}$$

1.3.3 Impurity effects on lifetime

There is a relationship between the lifetime and the majority carrier concentration. This is illustrated on figure 1.3.3 (11), where experimental values of n-type Si is plotted. In n-type, electrons are the majority carriers and holes the minority carriers.

Auger recombination is the dominant mechanism for high majority carrier densities in silicon. The Auger lifetime is given by equation 1.14 (11). C_n and C_p are the Auger recombination coefficients for electrons and holes, respectively.

$$\tau_{Aug} = \frac{1}{C_p(p_0^2 + 2p_0\Delta\mathrm{n} + \Delta n^2) + C_n(n_0^2 + 2n_0\Delta\mathrm{n} + \Delta n^2)} \tag{1.14}$$

SRH recombination is dominant for lower dopant concentrations. Equation 1.15 describes the lifetime due to SRH recombination (28; 11). n_1, p_1, τ_n and τ_p are described by the equations 1.16, 1.17 and 1.18, 1.19, respectively. υ_{th} is the thermal velocity given in equation 1.20, where m_{th} is the thermal electronic mass. n_i is the intrinsic carrier density, E_T is the trap energy level, and E_i is

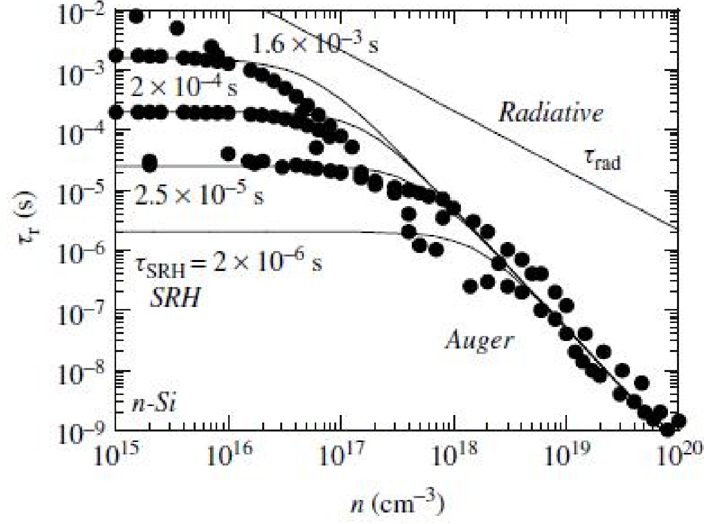

Figure 1.3.4: The graph shows a plot of lifetime vs. majority carrier concentration for n-type Si (11).

the ionization energy, k_B is the Boltzmann constant, T is the temperature, N_T is the trap density, σ_p and σ_n is the capture cross section for holes and electrons.

$$\tau_{SRH} = \frac{\tau_p(n_0 + n_1 + \Delta n) + \tau_n(p_0 + p_1 + \Delta p)}{p_0 + n_0 + \Delta n} \tag{1.15}$$

$$n_1 = n_i exp(\frac{E_T - E_i}{k_B T}) \tag{1.16}$$

$$p_1 = n_i exp(-\frac{E_T - E_i}{k_B T}) \tag{1.17}$$

$$\tau_n = \frac{1}{\sigma_n \upsilon_{th} N_T} \tag{1.18}$$

$$\tau_p = \frac{1}{\sigma_p \upsilon_{th} N_T} \tag{1.19}$$

$$\upsilon_{th} = \sqrt{8 k_B T / \pi m_{th}} \tag{1.20}$$

1.4 Crystal defects

Silicon crystallizes with the same structure as diamond, and defects in the atomic lattice structure generally have negative effects on the electrical behavior of a semiconductor. The three types of crystal defects that typically can be found in a Cz ingot are self-interstitials, vacancies and oxygen particles (29). The type of defect is dependent on the growth conditions, more specifically the temperature gradient G, and the growth rate V, where the temperature gradient is a spacial measure of the temperature variation (30).

1.4.1 Self interstitials and vacancies

There is a competition between self interstitial and vacancy defects in mono-Si (29). Although it is possible for them to exist close to one another, the probability that they will react and eliminate each other is high. If both types exist in the same ingot, they are usually found in different areas. V is constant throughout the cross section of an ingot, but G will vary. Areas where the relationship V/G is over a critical value $(V/G)_{cr}$, vacancies will dominate, and in areas under the critical value, interstitials will dominate.

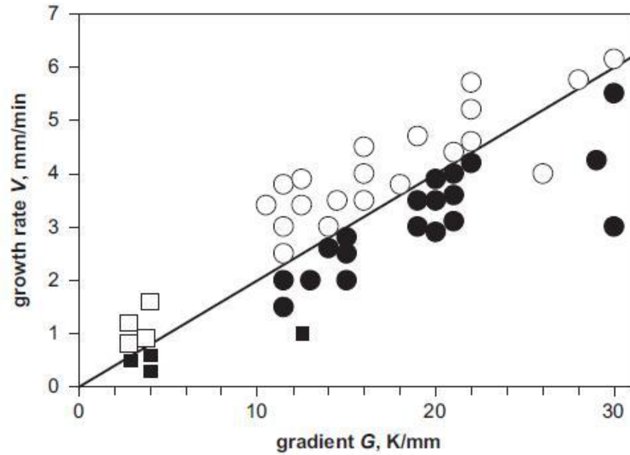

Figure 1.4.1: The V/G relationship. The diagonal curve is the critical value $(V/G)_{cr}$. The squares are values taken from the Cz process and the circles are from the Fz process. The black figures are interstitials and the empty ones are vacancies.

Control of the V/G ratio makes it possible to determine which type of defects to appear in the ingot (29). Figure 1.4.1 shows the critical value $(V/G)_{cr}$ for

Cz and Fz (float zone) monocrystals. The critical value can be described by equation 1.21.

$$(V/G)_{cr} = \frac{D_I C_{Ie}(E - \varepsilon_I) - D_V C_{Ve}(E - \varepsilon_V)}{kT_m^2(C_{Ve} - C_{Ie})} \quad (1.21)$$

D_I is the diffusivity of interstitials, D_V is the diffusivity of vacancies, C_{Ie} is the equilibrium interstitial concentration, C_{Ve} is the equilibrium vacancy concentration, E is energy of formation, ε_I is drift energy of interstitials, ε_V is drift energy of vacancies, k is the Boltzmann constant and T_m is the melting temperature.

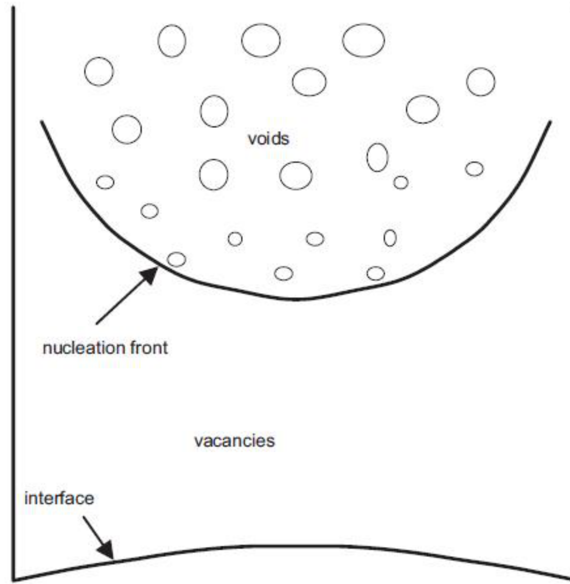

Figure 1.4.2: Nucleation of voids in a growing ingot. The higher T-region is populated only with vacancies, while the lower T-region contains voids. The two regions are separated by the nucleation front. The front is U-shape due to radial temperature differences (29).

Both vacancies and interstitials can agglomerate, and agglomerated vacancies are called voids. The nucleation of voids mainly happen within a short temperature interval, and the nucleation rate peaks around some nucleation temperature T_{nuc} (29). Within the temperature interval, the nucleation rate can become so high that the vacancy concentration drops due to the agglomeration. The voids will then dominate. The void density is controlled by the cooling rate $(-dT/dt)$

around T_{nuc}, and by the concentration of vacancies before agglomeration, C_{Vs}. In a growing ingot, the temperature difference between areas close to the solidification front and higher up in the ingot creates a boundary between where vacancies and voids dominate, as shown in figure 1.4.2. The boundary is U-shaped due to radial temperature differences in the ingot.

1.4.2 Oxygen particles

The oxygen is dissolved from the silica crucible, and can react with vacancies and voids (29). Having both vacancy and interstitial defects in the same ingot, the two areas are usually separated by a band of oxygen particles, as shown in the wafer on figure 1.4.3(29).

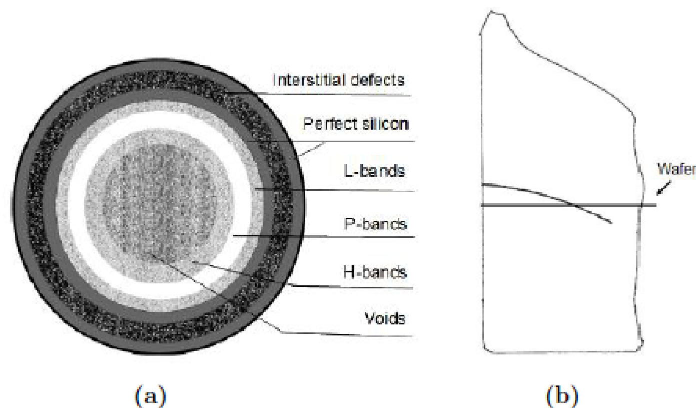

Figure 1.4.3: (a) shows how the bands appear on a wafer (29), and (b) shows how the wafer is cut from the ingot, where the curved line symbolizes the oxygen band. The P-band consists of large oxygen-void particles, while the L- and H-band consists of small oxygen vacancy particles.

In figure 1.4.3, the voids are located in the center, and the interstitial defects show up close to the edge of the ingot, but it can also be the other way around, depending on the V/G. The P-band consist of large oxygen-void particles, while the L- and H-bands consist of small oxygen-vacancy particles (29). Here, the interstitial region is surrounded by bands of perfect crystalline silicon.

The P-band has much lower oxygen concentrations than the L- and H-band because the amount of particles are a lot fewer here. There are two possible ways of which oxygen-void particles in the P-band are created (29). One is where

oxygen first reacts with vacancies, and then agglomerate into larger particles, having reduced the void nucleation energy barrier. They can also be created by oxygen reacting directly with voids, reducing the surface energy of the voids.

Void nucleation is actually enhanced by the oxygen (29). This is also why when vacancy concentration C_v is reduced, the nucleation rate of oxygen-void and -vacancy particles are less reduced than for voids. As C_v lowers from the vacancy region towards the interstitial region, oxygen particles is naturally positioned between the two areas.

1.5 Characterization methods

1.5.1 Cu-decoration

Copper decoration is a technique where $Cu(NO_3)_2$ solution is deposited onto the wafer, followed by heat treatment (31). This method has been shown to be fast and effective for expanding different kinds of defects in silicon, due to precipitation of the Cu during cooling. Secco etching can reveal these defects, so that they can be seen with the naked eye, or with a light microscope.

1.5.2 Oxygen concentration measurements

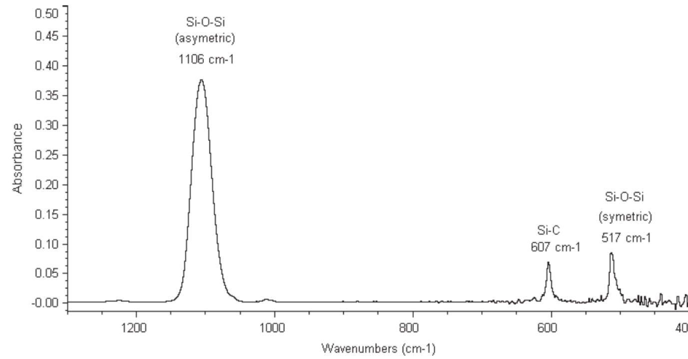

Figure 1.5.1: Absorbance spectrum of O_i from FTIR. The (Si-O_i-Si) bonds in the lattice absorb a fraction of the IR, which is proportional to the concentration of O_i, while the unbonded lattice Si is transparent to the IR wavelengths used (32).

Fourier Transform InfraRed spectroscopy (FTIR) can be used to identify interstitial oxygen (O_i) in Cz-Si. The silicon atoms form bonds with the interstitial oxygen atoms in the lattice in the form of (Si-O-Si) (32). These bonds absorb a portion of the infrared wavelengths used (2-25µm), while the unbonded Si is transparent. The amount of light absorbed is proportional to the concentration of bonded atoms, thus revealing the concentration of interstitial oxygen. The O_i i centered at a frequency of $1107cm^{-1}$, where frequency= $\frac{1}{wavelenght}$. Figure 1.5.1 shows the absorbance spectrum for O_i and C_s (substitutional carbon).

1.5.3 Resistivity measurements

The four point probe (FPP) is an instrument that measures the voltage induced by an applied current on the surface of a sample, which is then used to calculate the resistivity. The bulk resistivity ρ for a semi-infinite volume is described by equation 1.22, where s is the spacing between the probe needles in cm, V is the voltage measured in volts, I is the current measured in ampere (33).

$$\rho(\Omega\text{-cm}) = \frac{2\pi sV}{I} \tag{1.22}$$

If the sample thickness t is $<$ 5s, or the measurements are taken closer to an edge than 5s, the resistivity needs to be corrected with a correction factor a, as shown in equation 1.23 (33).. The correction factor a can be calculated from equation 1.24.

$$\rho(\Omega\text{-cm}) = \frac{2\pi sV}{I} * a \tag{1.23}$$

$$a = \frac{1}{1 + \frac{0.52632}{(t/s)^{1.9}}} \tag{1.24}$$

The standard deviation s between the measured and the calculated resistivity is given by equation 1.25 (34; 35), where y_i is the measured value, $f(x)$ the calculated value, n_{points} is the amount of points that were measured on, and $n_{parameters}$ is equal to 1.

$$s = \sqrt{\frac{\sum_{i=1}^{n_{points}} (y_i - f(x))^2}{n_{points} - n_{parameters}}} \tag{1.25}$$

1.5.4 Lifetime measurements with PCD

The photo conductance decay (PCD) lifetime characterization is the most common lifetime measurement technique for n-type Cz ingots (5). A photo conductance tool measured the conductivity within an area surrounded of a coil after a flash. The conductivity can be described by equation 1.26 (11). Here, μ_n is the mobility of electrons and μ_p for holes. q is the electronic charge, and the carrier densities for electrons and holes are given by $n = n_0 + \Delta n$ and $p = p_0 + \Delta p$, respectively.

$$\sigma = q(\mu_n n + \mu_p p) \tag{1.26}$$

Equation 1.26 can be modified to equation 1.27 for direct time-dependent excess carrier density measurements (11), where $\Delta\sigma_{ph}$ is the change in conductivity after a flash of light.

$$\Delta\sigma_{ph} = q(\mu_n \Delta n + \mu_p \Delta p) \tag{1.27}$$

The effective lifetime τ_{eff} can be described by equation 1.28. $G(t)$ is the generation rate of electron-hole pairs as a function of time. For thick samples, transient mode should be used. In this case, $G(t)$ is a small factor, and $G(t) << \frac{dn(t)}{dt}$ applies. Equation 1.28 can thus be modified into equation 1.31 for transient measurements.

$$\tau_{eff}(\Delta n) = \frac{\Delta n(t)}{G(t) - \frac{d\Delta n(t)}{dt}} \tag{1.28}$$

$$\tau_{eff}(\Delta n) = -\frac{\Delta n(t)}{\frac{d\Delta n(t)}{dt}} \tag{1.29}$$

The effective lifetime is a combination of recombination happening at the surface and in the bulk material, as described by equation 1.30 (11). For samples thicker than 1cm, τ_s can be neglected, and equation 1.30 can thus be modified to equation 1.31.

$$\frac{1}{\tau_{eff}} = \frac{1}{\tau_b} + \frac{1}{\tau_s} \tag{1.30}$$

$$\tau_{eff} = \tau_b \tag{1.31}$$

1.5.5 Lifetime measurements with CDI

CDI (carrier density imaging) (36) is a technique that gives a cartographic image of the lifetime of the sample. It is based on the free carrier absorption of IR-light in silicon. The instrument consists of a black body hotplate that emits IR radiation, and a fast CCD (charge coupled device) camera, which is sensitive to 3.5 – 5µm wavelengths.

The IR light from the hotplate is transmitted through the silicon sample under investigation, and the camera measures the transmission of the sample in two different states (36). The first state is when the sample is illuminated by a semiconductor laser that generates an excess free carrier density approximately equivalent to the generation at 1 sun (AM 1.5G). In the second state, the sample is in complete darkness, thus having no excess carrier generation.

The difference between the two images is proportional to the IR absorption of the excess free-carriers, and therefore to the *local* excess free carrier density $\Delta n(x, y)$. Since the generation $G(x, y)$ is known, the actual lifetimes for the different (x, y) positions on the sample $\tau_{eff}(x, y) = \frac{\Delta n(x,y)}{G(x,y)}$ can be calculated.

Chapter 2

Experimental

2.1 The samples

The ingot, named CZ2, was n-doped with phosphorous and created using the Cz method. It had a total length of ≈ 170 cm, and weighed 80 kg. The radius of the body was ≈ 16.5 - 17 cm. The rotation speed of the ingot was the same throughout the pulling. The pull speed for the top 50cm of the ingot is shown in figure 2.1.1. Figure 2.1.2 illustrates the ingot seen from above (not in scale), and how sample 1 was cut out. The other samples were cut out similarly.

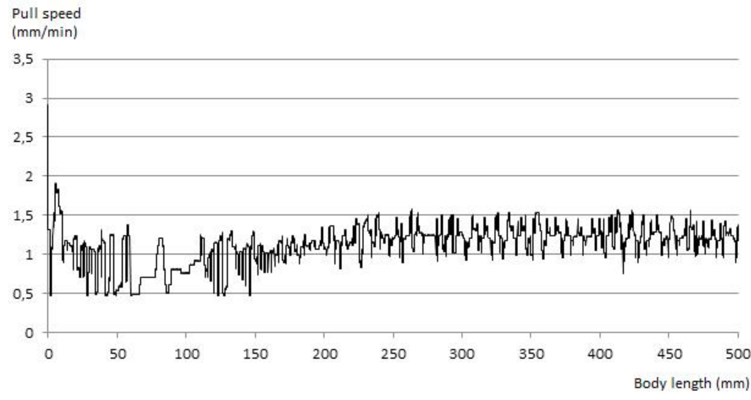

Figure 2.1.1: Pull speed for the first 50 cm of the n-doped Cz ingot

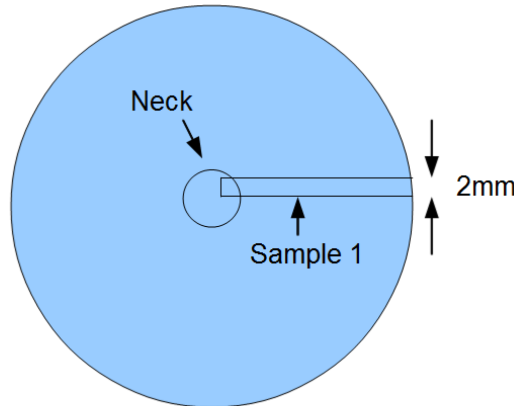

Figure 2.1.2: The ingot seen from above. The samples were cut out with a length of 17.5 cm from the shoulder, and with a radius of 7.5 - 8 cm. Sample 1 and 3 were 2 mm thick, and sample 4 and 5 were 2.5 mm thick.

5 samples were cut out of the ingot in total, but sample 2 was only used in V. Koien (2011) (37). They were all cut out vertically from the seed by a diamond saw, extending from a radius of 0 cm to approximately 7.5 − 8cm. The initial length of all the samples were 17.5 cm from the shoulder. The approximate shape of the samples are shown in figure 2.1.3, where the narrowing part to the left hand side is the crown, and the rest is a part of the body of the ingot. The dotted horizontal line is the center of the sample. Sample 1 plus sample 3 had a thickness of 2mm, and sample 4 and 5 was 2.5mm thick. Sample 3 was cut into an upper and lower half of 8cm and ≈ 9cm, respectively.

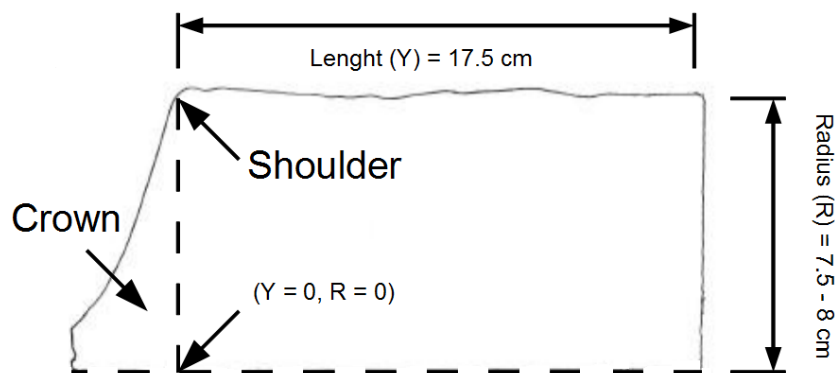

Figure 2.1.3: The surface of the samples. The crown is on the left hand side, with the end of the neck at the left bottom corner, and the shoulder at the top left corner.

Measurements overview:

- Sample 1:
  - Resistivity measurements after TD killing (FPP)
  - Oxygen measurements after TD killing (FTIR)
- Sample 3:
  - Oxygen measurements (FTIR)
  - Cu-decoration
- Sample 4:
  - Cu-decoration

- Sample 5:
  - Lifetime measurements before TD killing (CDI)
- Outside of the body:
  - Resistivity (FPP and PCD tool)
  - Lifetime (PCD tool)

2.2 Cu-decoration and etching

Sample 4 was cut into upper and lower halves (4a and 4b) 10 cm from the shoulder. Both parts were ground and polished (mechanically and chemically) down to a thickness below 1mm.

Procedure:

- RCA1 and RCA2 for 10min each to remove organic residues and oxides.
- Chemical polishing with CP4 for 30s.
- Secco etching for 30min.
- Wafers were rinsed for 5 min into 1M solution of $Cu(NO_3)_2$ with addition of HF acid = 24.16g/100m
- Spreading solution on samples and baking it at 50 - 60 ºC until it turned to powder (around 3 to 4 hours).
- Heating of the $Cu(NO_3)_2$ covered samples at 900 ºC for 30min on quartz tubes to avoid contamination.
- Chemical polishing with CP4 to remove the residue powder.
- Secco etching for 30 min.

Chemicals used:

- Cu decoration: 3 mol/l (M) solution of copper nitrate $Cu(NO_3)2\textbf{.}3H_2O = 72.48/100ml$
- RCA1: $1:1:5 = H_2O_2 : NH_4OH :$ DI water
- RCA 2: $1:1:6 = H_2O_2 :$ HCl : DI water
- CP4: HNO_3 (69wt%) : HF (49wt%) : CH_3COOH (99.9 wt%) = 5:3:3
- Secco etch: HF (49%) : $K_2Cr_2O_7$ (4.41g/100ml) = 2 : 1

2.3 Oxygen measurements

Sample 1 was measured on after thermal donor killing and mechanical polishing down to 1µm. Sample 4 was measured on with no heat treatment after chemical polishing with CP4. The measurements were done on each cm^2 from 1cm below the shoulder and 1cm from the center of the ingot. On sample 4, only $R = 7$ was measured.

2.4 Resistivity measurements

After thermal donor killing, the resistivity was measured on every cm^2 on the surface of sample 1 below the shoulder. Resistivity measurements were also taken on every 10th cm on the outside of the ingot from 30-160cm below the shoulder. The probe distance s was 0.635 mm, making 5s equal to 5s = 3.18mm. Since t < 5s, correction was needed. Equation 2.1 calculates a from equation 1.24. The distance to nearest edge was never smaller than 0.5 cm, and since 0.5cm > 5s, no additional correction was needed for the measurements close to the edge.

$$a = \frac{1}{1 + \frac{0.52632}{(2mm/0.635mm)^{1.9}}} = 0.94 \tag{2.1}$$

2.5 Lifetime measurements

2.5.1 PCD

The coil was to approximately $4cm$ in length and $1cm$ in width, making up an area of $4cm^2$. The measurements gives the average conductivity within the area of the coil. The measurements were taken on sample 2, which did not need surface passivation due to it's thickness of 3.5cm > 1cm. Transient mode was used. The injection level was $5 * 10^{14}$. The lifetime was also registered on the outside of the ingot from 30 cm from the shoulder and below. An average resistivity of 2Ω for the sample was plotted into the software of the PCD tool, as small variations in resistivity do not affect the results (38). Using equation 1.28 (39; 11) and the measured value Δn, the PCD tool gave the effective lifetime τ_{eff} for the different sections measured on.

2.5.2 CDI

The sample was prepared before passivation with the following method:

1. Deionized (DI) water cleaning, 5min
2. RCA1 at 75ºC, 10 min
   - $1:1:5 = H_2O_2 : NH_4OH :$ DI water
3. RCA2 at 75ºC, 10min
   - $1:1:6 = H_2O_2 :$ HCl : DI water
4. Chemical polishing 4
   - $5:3:3 =$HF : $HNO_3 : CH_3COOH$

The samples were surface passivated with SiH_4 using plasma enhanced chemical vapour deposition (PECVD) with the following parameters:

- 30 sccm
- $T = 225$ºC
- $t = 1.5$min
- $P = 450$mTorr
- Thickness of deposition= 30nm (on each side)
- Plasma frequency = 135mHz

Chapter 3

Results

3.1 Cu-decoration and etching

Figure 3.1.1 shows the etch pits of sample 3a after copper decoration and secco etching. The dot disturbances on the otherwise smooth surface are the defects revealed. The center of the ingot is at the bottom on the images. The crown is on the left of hand side. Some scratch marks from the polishing are visible on both samples. The samples were also both cracked in one corner. A larger image of the sample can be found in appendix 1 and 2. The Cu decoration of sample 3b was unsuccessful, and is shown in Appendix 2 and 5.

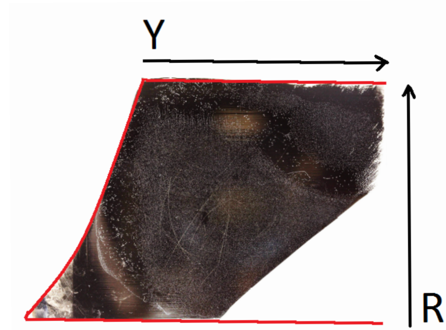

Figure 3.1.1: Sample 3a. The red outline shows the original shape of the sample. The center of the ingot is at the bottom on the images. The crown is on the left of hand side of sample 3a. The center part of the surface of 3a is full of small, dense particles. Outside this area, there is a relatively clear band that has a few larger, more spread particles. The band arches inwards from around 4 cm, separating the inner dense area with another area with small dense particles close to the edge.

Sample 3a seems to be relatively defect free in the top crown area. The center area of the surface has a relatively large density of small particles. In the transition between band area and the particle dominated area, there are some larger particles that are much more spread. The same is true for the edge of the ingot on sample 3a. There is also a relative clear band with a few large defects on it, arching inwards from around 4cm. This band separates the center area with another area of densely lying smaller particles, closer to the edge.

Figure 4.5.1 and 3.1.3 shows the defect patterns from the top and bottom parts on sample 4, respectively. In contrast to figure 3.1.1, the band outside the “bubble” seems to have a high density of defects, while the “bubble” itself seems to have less defects. However, some clear spots can also be seen close to the edge above the “bubble”. In the very center of the ingot, the density seems to be very high from about the same height as the “bubble”.

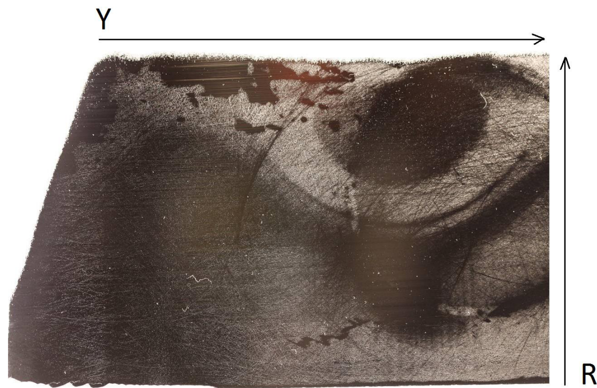

Figure 3.1.2: Sample 4, top. Defect density seems to be very high in the center of the ingot at about the same length as where the “bubble” starts. The band surrounding the bubble also seem to have a high defect density.

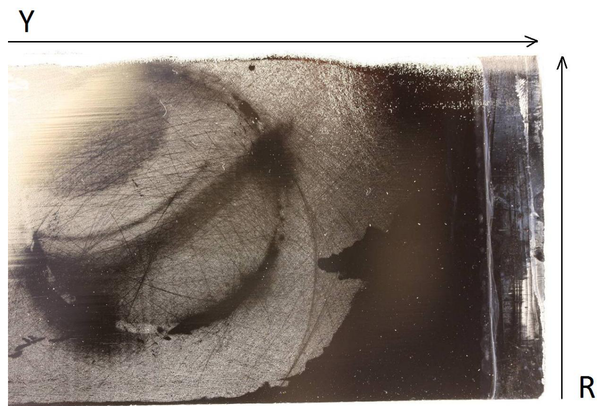

Figure 3.1.3: Sample 4, bottom. A thin, circular shape seems to interrupt the defect pattern. Very fiew defects can be found at the bottom of the sample (right hand side). The last cm of the sample was usufficiently submerged in the acid.

Categorization of the defects, illustrated by figure 3.1.4:

a) illustrates a large defect, which has a diameter > 100µm

b) illustrates a small defect, which has a diameter < 100µm

c) illustrates a cross-shaped defect

Figure 3.1.4: Definition of the defects: a) large defect, b) small defect, c) cross-shaped defect.

3.1.1 Microscopy images, sample 3

Figure3.1.5 was taken inside the band that surrounds the “bubble”. These particles are relatively large, and look like they are made from smaller particles that have clustered. Figure 3.1.6 is taken from the large center area with small, dense particles. Some of the defects are dot-like, and some are shaped like crosses.

Figure 3.1.7 is taken in the transition area where the large, spread particles meed the small dense defects. The small, dense defects shown here is from other side of the belt of the large, dense defect dominated area in the center of the sample. The image illustrates similar particles to those in figure 3.1.5 on the left hand side, and defects similar to those in figure 3.1.6 on the right hand side.

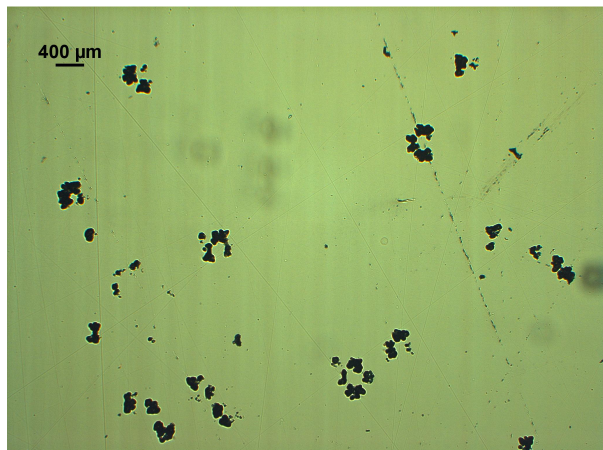

Figure 3.1.5: $Y \approx 5$cm, $R \approx 5$cm. These particles are relatively large, and are not as densely distributed as the small defect dominated areas. This was taken inside the band surrounding the bubble. The defects here look like they are made from clusters of small defects.

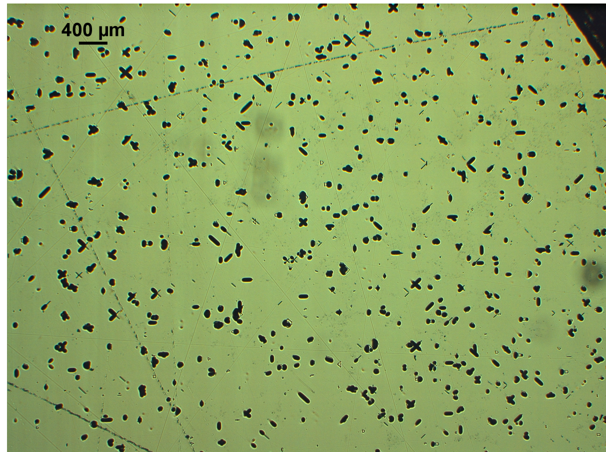

Figure 3.1.6: $Y \approx 5$, $R \approx 4$. This is from the large central area outside the "bubble", with small, dense particles. Some of the defects are dot-like, and some are shaped like crosses.

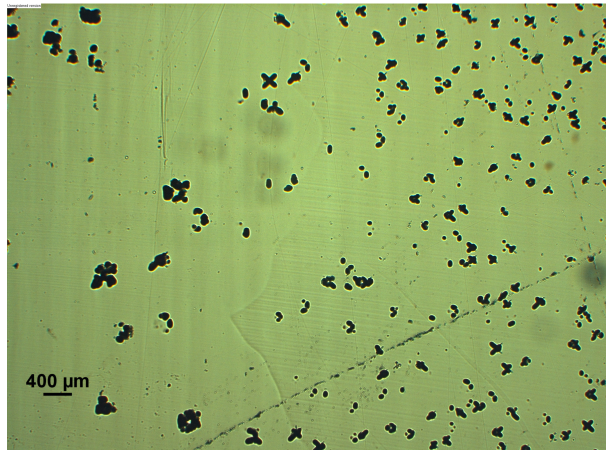

Figure 3.1.7: $Y \approx 4$cm, edge. Here, there is a transition area between an area of small, dense defects (right) and large, more spread defects (left), representing the beginning of the "bubble". The defects have the shape of dots and crosses.

The results from below 8cm (samlpe 3b) were found to be corrupted due to surface defects and/or insufficient Cu diffusion. Examples of the results are illustrated in Appendix 3.

3.1.2 Microscopy images, sample 4

Figure 3.1.8 and 3.1.9 shows the defects inside the "bubble" and the transition from the bubble to the band surrounding the band, respectively.

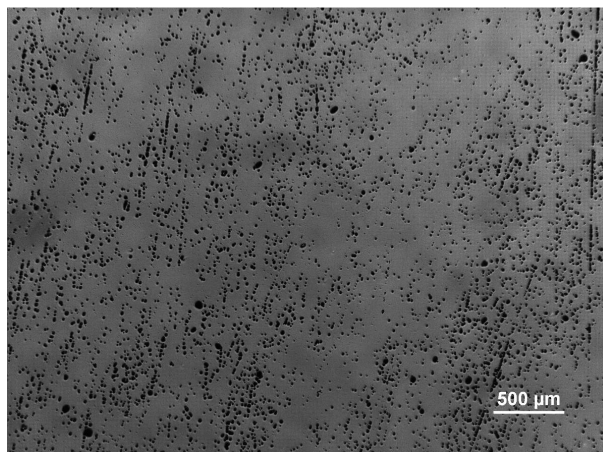

Figure 3.1.8: Inside the "bubble". The defect density seems to be more irregular than inside the bubble of sample 3a, shown in figure 3.1.7.

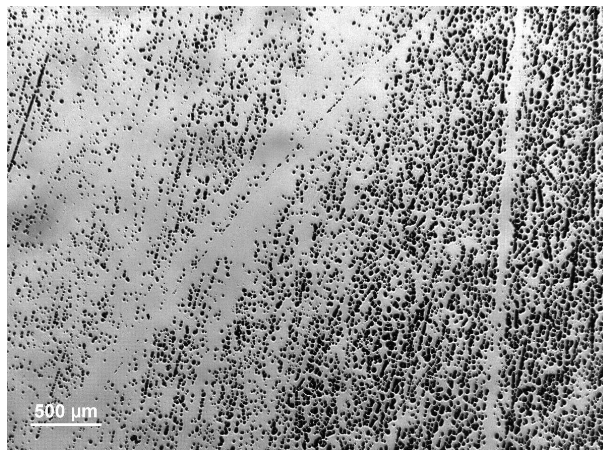

Figure 3.1.9: Transition from the "bubble" (left) to the band surrounding the "bubble" (right). The defect concentration seems to be much higher in the band.

Figure 3.1.10 shows the high density area at about the same hight as the "bubble", in the very center of the sample. The defect density here is medium, compared to the two areas shown in figure 3.1.9.

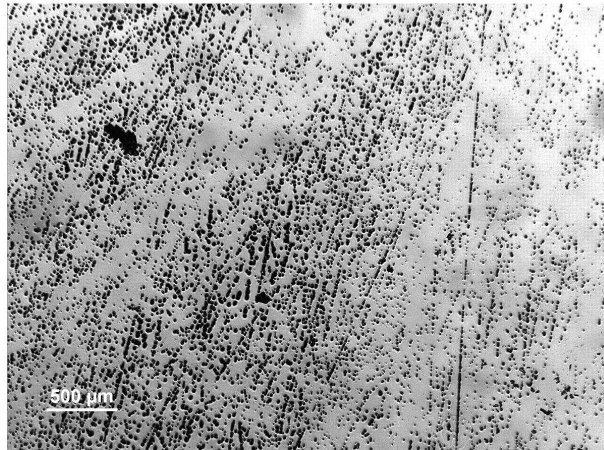

Figure 3.1.10: Vacancy rich area. The concentration seems to be higher than inside the “bubble”, but lower than in the surrounding band.

The defect density seems to be relatively low inside the “bubble”, and much higher in the band, opposite of what was revealed from sample 3. Compared to sample 3a, however, the defect density inside the “bubble” seems to be high, and more irregularly distributed. The defect dense zones in sample 4 also seem to be even denser than in sample 3.

3.1.3 CDI, sample 4

Figure 3.1.11, 3.1.12, 3.1.13, shows the top, bottom and the entire sample after Cu decoration, respectively. The CDI reveals the difference in defect density, as the lifetime is reduced by the Cu. Red color symbolizes high lifetime and low Cu density, green is medium lifetime and Cu density, Blue is low lifetime, meaning a high Cu density. The dark blue color is not a part of the sample.

On figure 3.1.11, the crown is to the left, the edge is at the top of the image, and the center is at the bottom of the image. The Cu density seems to be small in the crown and at the edge of the ingot. There is a high lifetime “bubble” close to the edge on the right hand side of the image, which seems to be enclosed by a band that stretches from the crown and along the edge of the ingot. Inside this band, there seems to be a low lifetime band. Inside the blue low lifetime band, there is an area that seems to be of medium high Cu density.

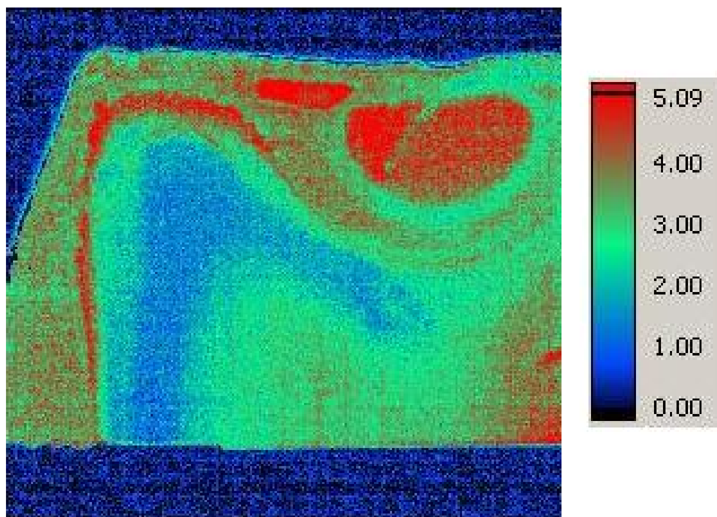

Figure 3.1.11: At the edge, the lifetime is relatively high, in other words, the Cu density seems to be low. The "bubble" has very high lifetime. The lowest lifetime is at the blue band, which lies inside the red edge band. Inside the blue band, there seems to be an area of medium Cu density.

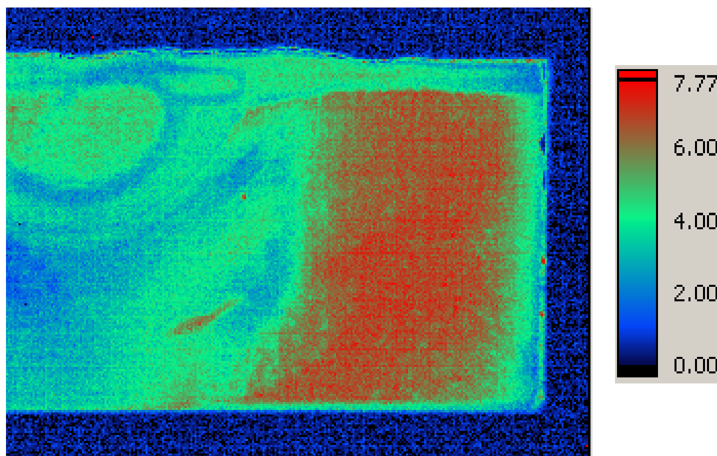

Figure 3.1.12: The lifetime scale is a little higher here than in figure 3.1.12, making the parts of the ingot shown in figure 3.1.12 look more green and blue. There is a sharp transition to a high lifetime area at the bottom of the sample. The lifetime here is more uniform than higher up in the ingot.

On figure 3.1.12, there seems to be a high lifetime/low Cu density area at the bottom of the sample (on the right hand side). Compared to the lifetime inside

the “bubble” and at the edge (here on the left hand side) seen further up on the sample, the Cu density seems to be significantly much higher here. The relative lifetime is higher here than in figure 3.1.11. Hence, the bubble looks more green.

On figure 3.1.13, the lifetime spectrum is the same throughout the image, which shows the entire sample 4. As seen in figure 3.1.12, the lifetime at the bottom of the sample (right hand side) is higher than the lifetime at the edge. This is also an area with few defect patters, with the exception of a thin band at the edge (at the top of the image on the right hand side).

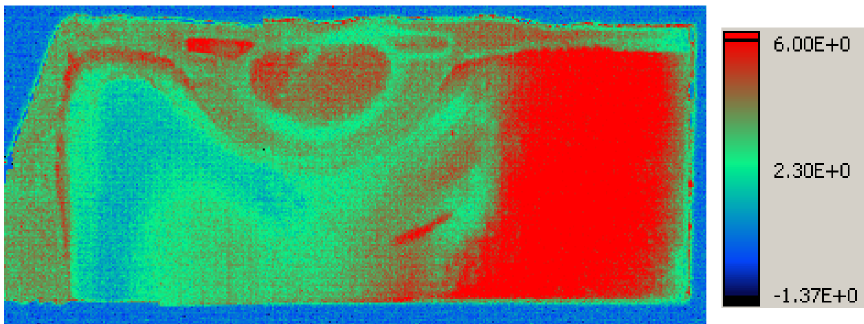

Figure 3.1.13: The top and bottom parts in one. The lifetime at the bottom of the sample is clearly much higher than in the top part.

3.2 Oxygen concentration

Figure 3.2.1 and 3.2.2 shows the plots for the O_i concentration in a lengthwise and radial perspective, respectively. The concentration only changes a little with length. Figure 3.2.2 shows that for $R > 5$ the concentration drops. This can be also be seen on figure 3.2.1, where $R = 6$ and $R = 7$ have much lower values than the smaller radiuses. $R = 7$ is about twice as low as $R = 6$, and both are much more unstable than the smaller radiuses.

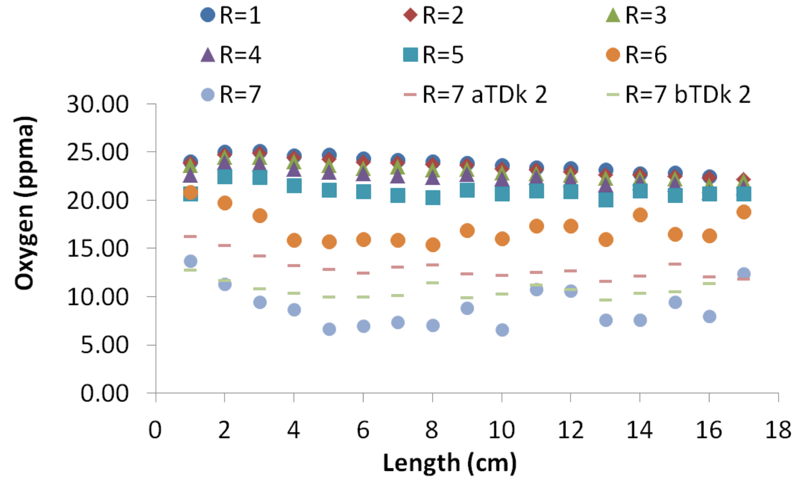

Figure 3.2.1: Oxygen concentration after TD-killing for different radiuses plotted vs. length. The amount of O_i is slightly reducing with increasing length. The plot sequences $R = 1 - 5$ are all pretty similar for each length, but the sequences $R = 6$ and $R = 7$ are increasingly much lower, and also more unstable lengthwise. $R = 7$ aTDk 2 is a second measurement of $R = 7$ on the heat treated sample, an $R = 7$ bTDk is a measurement on the same radius from sample 4 with no heat treatment.

The instability can also be seen from the spread of the points for $R = 6$ and $R = 7$ in figure 3.2.2, which is larger than the spread on the smaller radiuses. On figure 3.2.1, $R = 7$ aTDk 2 is a second measurement of $R = 7$, and $R = 7$ bTDk is from sample 4 without heat treatment. $R = 7$ aTDk 2 has higher values than both $R = 7$ and $R = 7$ aTDk 2. Both are higher than $R = 7$, and $R = 7$ aTDk 2 has the highest concentrations.

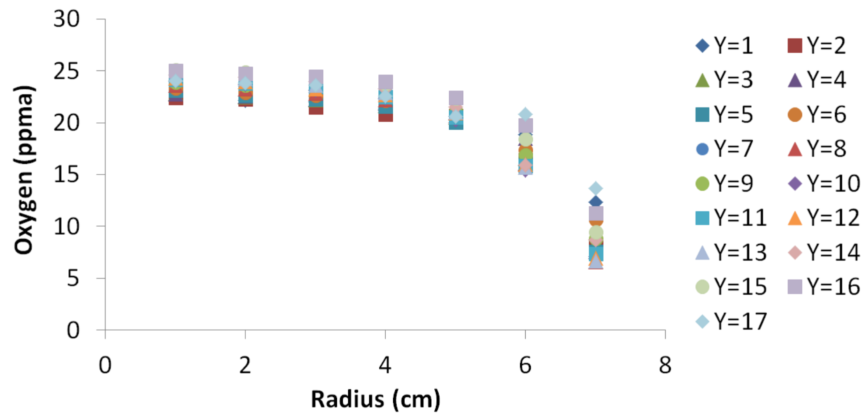

Figure 3.2.2: Oxygen concentration after TD-killing for different lengths plotted vs. radius. For all the lengths, the oxygen concentration drops towards the edge after $R = 5$. The spread between the dots of the different lengths is a little higher for $R = 6$ and $R = 7$ than for the smaller radiuses.

3.3 Resistivity

Using a current $I = 5mA$, the first measurement gave a voltage of 62 mV. The resistivity was calculated as shown in equation 3.1. Figure 3.3.1 and 3.3.2 show the resistivity measurements after TD-killing, plotted vs. length and radius, respectively.

$$\rho = \frac{2\pi * 0.635 * 62mV}{5mA} * 0.94 = 4.65(\Omega - cm) \tag{3.1}$$

On figure 3.3.1, the trend line Linear ($R = 1$) and Linear ($R = 4$) show that the trend for both radiuses is decreasing resistivity with increasing length. In figure 3.3.2, the trend lines are more unstable. For Linear ($R = 1$), the trend is decreasing resistivity with increasing length. For Linear ($R = 3$), the trend line is flat, and for radiuses higher than this, the trend lines indicate increasing resistivity.

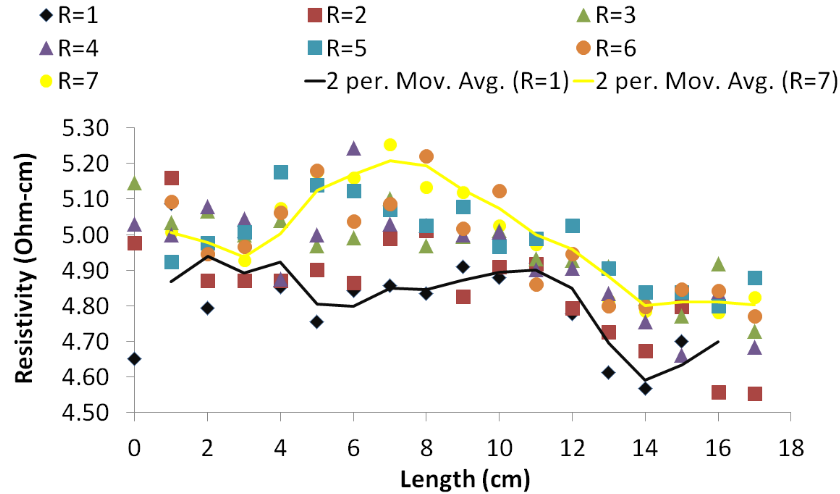

Figure 3.3.1: Resistivity measurements plotted vs. length for different radiuses after TD-killing. The moving average trend lines show a trend of decreasing resistivity with increasing length after 12cm. .

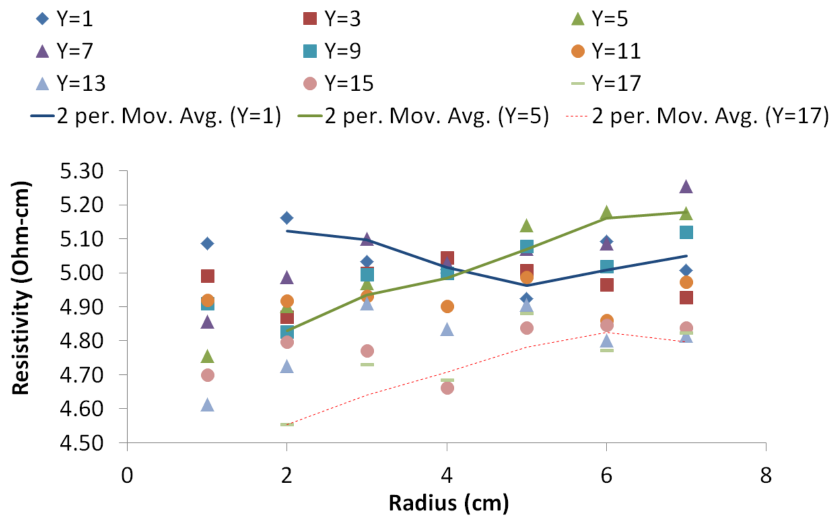

Figure 3.3.2: Resistivity measurements plotted vs. radius for different lengths after TD-killing. The moving average plots shows that the general trend is the resistivity going up with increasing radius.

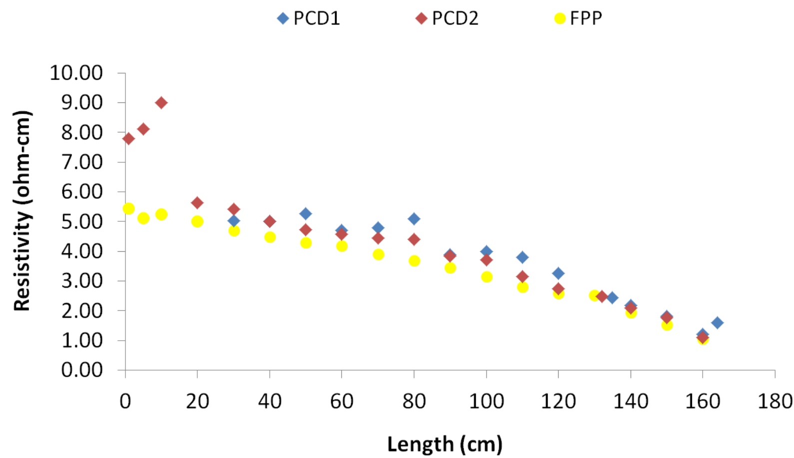

Figure 3.3.3: Resistivity measured on the outside of the ingot. The results from both the FPP and the photoconductance tool are plotted. Both results show a decreasing trend. In the top part, the FPP and PCD measurements deviate significantly from each other.

Figure 3.3.3 shows the plot after resistivity measurements taken with FPP and with the PCD tool taken on the outside of the ingot. The descending trend is similar, but the first three points have very different values. The plot from the PCD tool is also a little more irregular than that of the FPP.

3.4 Lifetime

Figure 3.4.1 shows the effective lifetime measurements taken on the outside of the ingot between. The coil started at the given lengths, and stretched 4cm in length from this. “PCD1” were done simultaneously with “PCD1” in figure 3.3.3 and “PCD2” equally correspond to “PCD2”. The lifetime is decreasing with increasing length of the ingot, except during the 5 first cm, where it increases.

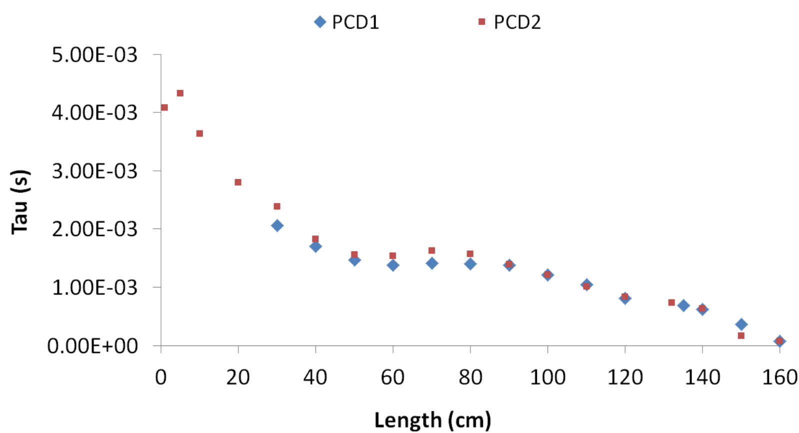

Figure 3.4.1: Lifetime measured by the PCD tool on outside of the ingot. The lifetime is decreasing with increasing length. Both curves are relatively flat between $60 - 90$cm.

Figure 3.4.2 shows the CDI of sample 5a, which was 8cm long. Red symbolizes the highest lifetime, green is medium and blue is low lifetime. The dark blue and black area is not a part of the sample. In the crown part, the lifetime is relatively high. There is a central zone where the lifetime is very low.

Inside this zone, in the most central parts of the ingot at about $Y = 2$cm, there is a small zone with a slightly increased lifetime. There is an outer layer with high lifetime stretching from the edge of the ingot. It curves inwards increasing from about 1.5cm to about 4cm from the edge towards the center. The transition from low to high lifetime is relatively abrupt in the first $3 - 4$cm of the sample.

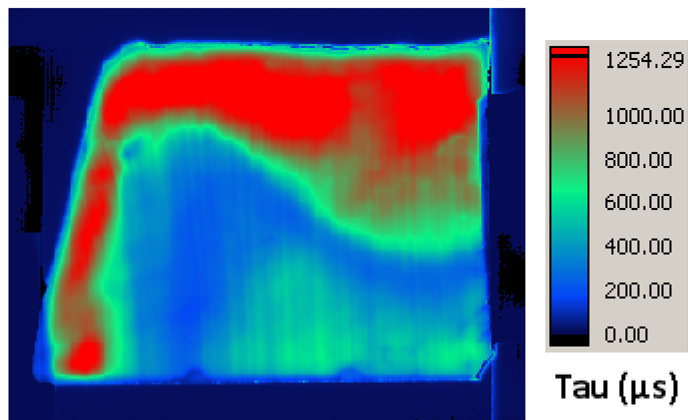

Figure 3.4.2: Red symbolizes the highest lifetime, green is medium and blue is low lifetime. Above the shoulder, the lifetime is relatively high. There is a large central zone where the lifetime is very low. Inside this zone, in the most central parts of the ingot at about $Y = 2 - 3$cm, there is a small zone with a slightly increased lifetime. There is an outer layer with high lifetime that stretches inwards from the edge of the ingot. It curves towards the center, increasing from about 1.5cm to about 4cm from the edge with increasing length. The transition from low to high lifetime is relatively abrupt in the first 3-4cm of the sample. The dark blue and black area is the background, and thus not a part of the sample.

Chapter 4

Discussion

4.1 Etch defects

In a typical Cz ingot, there is a transition from an interstitial dominated to a vacancy dominated area moving downwards in the ingot, separated by a P-band. In CZ2, no P-band seems to be present either in figure 3.1.2 or 3.1.1. The defect pattern on sample 4, shown in figure 3.1.2, is different, almost opposite of the defect pattern in figure 3.1.1, which shows sample 3. The “bubble”, as well as a similar contrast pattern can be see in both samples.

In figure 3.1.1, the band surrounding the bubble seems to be a perfect crystalline region, while in figure 3.1.2, this band is full of densely distributed defects. Inside the “bubble”, the two samples seem to have a similar, but opposite defect distribution, as figure 3.1.1 and 3.1.9 show a “bubble” full of defects, while figure 3.1.2 and 3.1.7 show a “bubble” with fewer defects, compared to the band surrounding it.

A CDI of the Cu decorated sample is another way of revealing the most defect dense areas. As Cu reacts with defects, the Cu has contaminated the high defect density areas the most, thus decreasing in lifetime the most in these areas. On figure 3.1.13 and 3.1.12, the lifetime seems to increase rapidly from around 12cm. In this area, there is no apparent defect contrast, which is unexpected, as the lifetime patterns stop abruptly here. It is likely that the Cu decoration was unsuccessful in this area. Other possible explanations is that the area is either defect free or dominated by only one type of defects.

Figure 4.1.1 shows figure 3.1.11 and figure 3.1.2 put together. The CDI image of sample 4 suggests a different defect density distribution than the defect patterns from the same sample. The CDI show a low lifetime/high density zone in a band situated inside the high lifetime band at the edge, which also encloses the “bubble”.

This is not consistent with the high defect level found in the same band, which may suggest that the preferential etching was unsuccessful. There are also some sharp disruptions in the defect pattern that is not consistent with the CDI pattern, which thus cannot be explained by unsuccessful diffusion of Cu. Hence, the etching process may be the cause. The spots in the defect pattern may be an indication that the defects in the band on figure 4.1.1, which appears more crystalline in figure 3.1.1, are in fact surface defects, as the surface look more crystalline within the spots. However, the reason for these possible surface defects is unknown, and should be further investigated.

Also, the low lifetime band seen in the CDI does not correspond to the high defect density found in the same area. The same is true for the very center of the ingot. The CDI defects seem to be almost opposite of the defects revealed by the preferential etching, with the exception of the “bubble”, where the high

lifetime actually corresponds to the low defect density found. The reason for this unexpected correlation between the CDI and the same sample after preferential etching is unknown, and should be further investigated. It may be due to an unfortunate diffusion process, as well as an unsuccessful etch process.

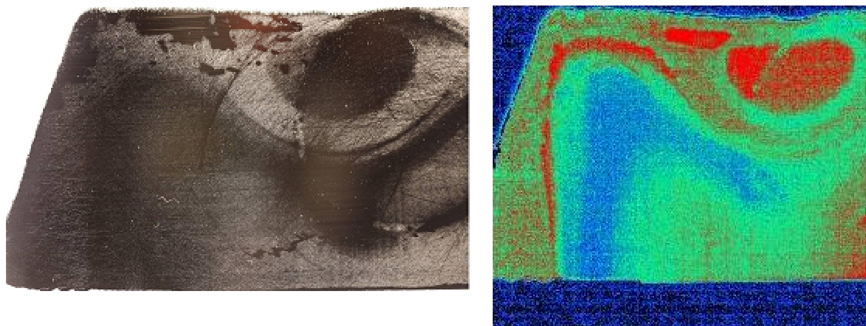

Figure 4.1.1: The defect pattern of sample 4 is shown to the left, the right image is the CDI of the same sample. The images are also shown in figure 3.1.2 and 3.1.11, respectively. The correspondence between the CDI and the sample after preferential etching seems to be inverse, as the high defect areas have high lifetime in the CDI. This is opposite of what was expected. The exception is the “bubble”, in which the lifetime and defect density is correlating. However, the condition in the “bubble” is opposite of what was found in sample 3.

Figure 4.1.2 shows the CDI of the 8 cm long sample 3a after Cu decoration, taken from V. Koien (2011) (37). The patterns on the CDI of sample 3a matches the defect pattern on figure 3.1.1 very well, showing a sharp contrast between the different areas. Here, even the high defect density found in the “bubble” corresponds to the low lifetime in the CDI.

Compared to figure 3.1.13, the trend in the CDI is mostly the same, except for the high lifetime found in the “bubble” on sample 4, which is a low lifetime area on sample 3a. This, along with the correspondence between defects and CDI lifetime, suggests that sample 3 is a more “trustworthy” candidate than sample 4, especially at the edge. The following discussion is therefore based on the assumption that sample 3a reveals the true defect pattern of the ingot.

On figure 2.1.1, the “bubble” seems to correspond to the low growth rate part in the pulling parameters graph. Assuming a steady temperature gradient G, the V/G ratio is believed to be relatively low here, causing a transition towards what is most likely interstitials. Thus, the central regions of the ingot are believed to be vacancy dominated. Looking at the defects pattern on sample 3, the band separating the two is likely to be a perfect crystalline band, with the exception of

a few large defects. It is also possible that this is a self interstitial rich area, and that the difference between the “bubble” and the band surrounding it is a higher degree of clustering inside the “bubble”. However, no defects were revealed by the Cu decoration in the band, which argues for a more perfect crystalline area.

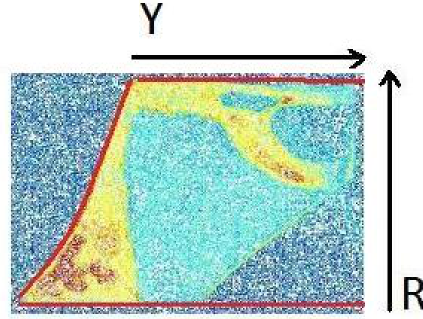

Figure 4.1.2: CDI of sample 3a, taken from V. Koien (2011) (37). The red outline shows the original shape of the sample. Both samples were cracked at the bottom inner corner. The red area on the sample has the highest lifetime, and the blue area has the lowest. The dark blue area is not part of the sample.

During the first 4 cm, the assumed perfect crystalline band surrounding the “bubble” lies steady at the edge of the ingot. Around 4cm, the band starts to bend inwards on sample 3a, before it curves back towards the edge again, enclosing the “bubble”. This is also consistent with the growth parameters on figure 2.1.1, which lowers, the increases again before it stabilizes at relatively same lengths as the “bubble”. From figure 2.1.1, showing the pull speed data V, it can be seen that in the first $\approx$ 3cm the pull speed is relatively high. Around 4cm it is very unstable, and after 6cm the average pull speed is relatively low. From 10cm, the average speed then slowly stabilizes towards 1.2 - 1.3 mm/min, where it is stable in average between 20cm - 50cm.

Regarding the center parts of the CDIs of the two samples, shown in figure 3.1.11 and 4.1.2, both samples seem to have a low lifetime here. In sample 4, based on the CDI, the defect density seems to decrease in the most central parts of the ingot, as discussed previously. The lifetime contrast is higher for sample 4, at it is possible that the lifetime (or defect density) here, despite the deviation in the “bubble”, is correct. In this case, figure 3.1.11 may in fact be revealing a transition from vacancies to voids, as the lifetime in the CDI of sample 4 increases towards the center of the ingot at about the same height as the “bubble”. It is also possible that the low lifetime band outside this assumed void region is an H- or L-band.

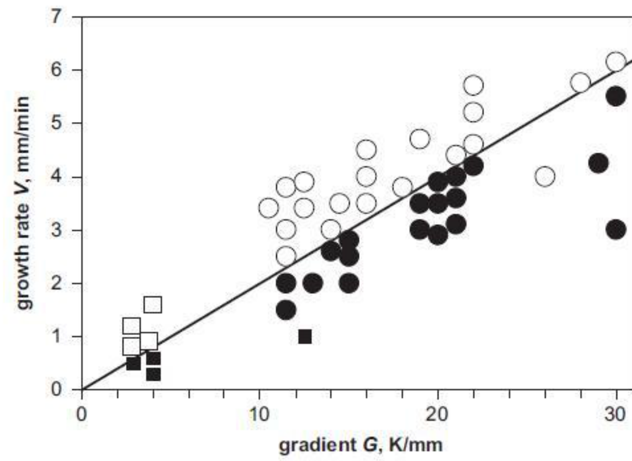

Figure 4.1.3: The V/G relationship, also illustrated in figure 1.4.1. The black figures are interstitials and the empty ones are vacancies. The “bubble” seems to correlate with a low V/G ratio, suggesting that this is a self interstitial dominated area.

4.2 Oxygen distribution

Figure 4.2.1 shows a comparison of the oxygen level measured before (bTDk) and after (aTDk) thermal donor killing of a radius of $R = 2$, and $R = 7$cm. 7cm bTDk is taken from V. Koien (2011) (37). For $R = 2$, the results both before and after thermal donor killing gave a similar small decrease with increasing length, which was expected.

There is a small relatively stable gap between $R = 7$ bTDk and $R = 7$ bTDk 2. The gap between $R = 7$ aTDk and $R = 7$ aTDk 2 is more than twice as large on some points, but the size of it is more unstable. Also, $R = 7$ bTDk has higher values than $R = 7$ aTDk, a.i. the heat treated measurements has larger concentrations than after the heat treatment, which suggest that the heat treatment removed some of the oxygen.

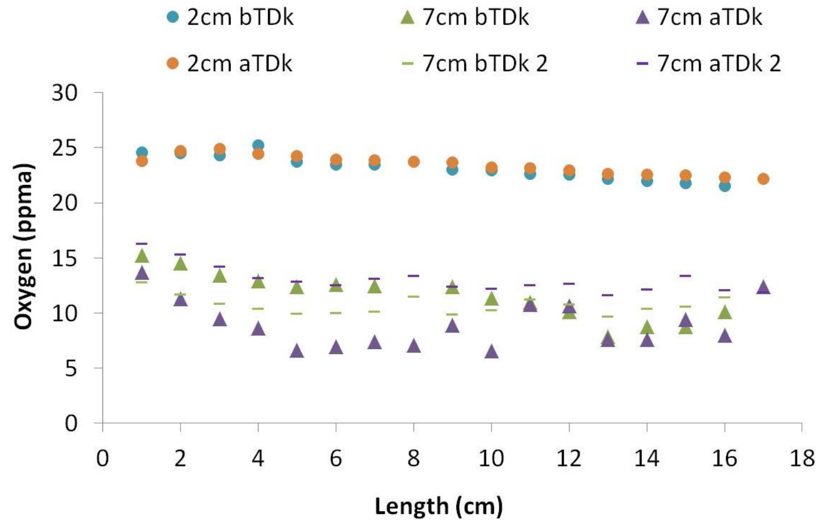

Figure 4.2.1: Oxygen concentration before (bTDk) and after (aTDk) thermal donor killing for the radiuses $R = 2$cm and $R = 7$cm vs. length.

On the other hand, looking at $R = 7$ bTDk 2 and $R = 7$ aTDk 2, the concentration is higher after thermal donor killing. The most likely explanation is that the concentration was not changed by the heat treatment, and that the concentration variations on the measurements from $R = 6$ and $R = 7$ is that the concentration changes rapidly here, as seen on figure 3.2.2, and even small differences in position involve relatively large differences in the concentration.

Moreover, if the oxygen concentration had been changed by the thermal donor killing found in V. Koien (2011) (37), the biggest difference in oxygen concentration should have been in the center of the ingot, were the thermal donor concentration was the highest. Looking at $R = 2$ before and after TDk, which have very similar values, this was not the case.

In W. Wijaranakula (40), a decrease in O_i of $12.5-14.3\%$ ($1-C_i/C_{i0}$, where C_i is the concentration of O_i and C_{i0} is the initial O_i concentration before annealing) was reported when annealing at $460-470$°C for 64h to create thermal donors. A similar increase in O_i would be expected after thermal donor killing. Assuming $C_i = 25$ppma and a change of 12.5%, the concentration after thermal donor killing is thus expected to be $C_{i0} = 25/(1-0.125) = 28.6$ppma. Experimental measurements vs. a standard sample gave a variation of ± 0.1 ppma.

In W. Wijaranakula, the oxygen concentration were about $10^{17}cm^{-3}$. By multiplying with Avogadro's number ($6.0221415 * 10^{23}cm^{-3}$, (41)), the concentration at $R = 1$ was calculated to $25*10^{-6}atoms/atoms*6.0221415*10^{23}atoms/cm^3 \approx 1.5*10^{19}$. Still, an increase in O_i is expected after thermal donor killing. A possible explanation may be that the oxygen was more uniform in W. Wijaranakula, and that diffusion towards the sides may have happened in CZ2.

In the case of nonuniform oxygen concentration in both ingots, the higher concentration in CZ2 may have lead to a higher redistribution of oxygen, leading to diffusion towards the sides. It is also possible that chemical polishing with CP4 was insufficient for sample preparation, and that mechanical grinding and polishing should be done in prior.

4.3 Resistivity measurements

In V. Koien (2011) (37), the resistivity was measured before thermal donor killing. Figure 4.3.1 and 4.3.2 shows these results before TD-killing plotted vs. length and radius, respectively.

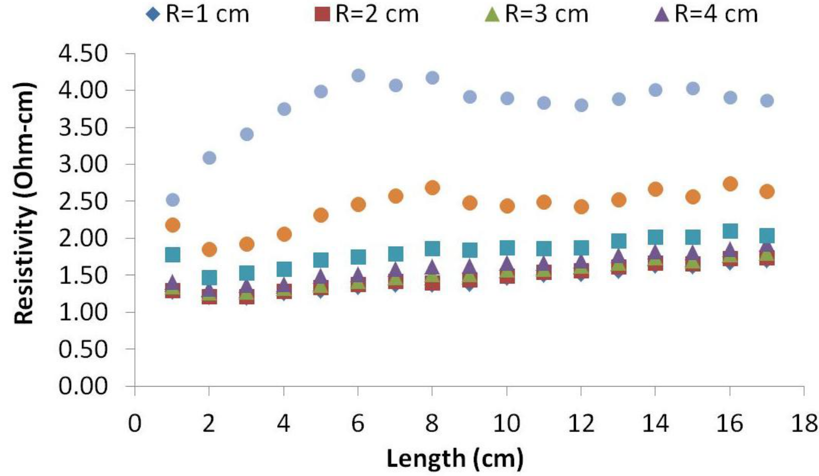

Figure 4.3.1: Resistivity measurements plotted vs. length for different radiuses before TD-killing, (37).

Compared to figure 3.3.1, figure 4.3.1, taken before thermal donor killing, shows much more stable results, where there is a clear individual increase in resistivity with length for each radius. On figure 3.3.1, measured after thermal donor killing, the measurements are unstable, both between the different radiuses and for the change lengthwise. However, the overall difference in resistivity is much larger than for figure 3.3.1, varying between 1.2 and 4.2 Ω-cm, whereas the variation after thermal donor killing is between 4.6 and 5.3 Ω-cm.

The small variation of 0.7 between the highest and lowest measurement, compared to 3.0 on figure 4.3.1, indicate that the measurements taken after thermal donor killing is still relatively stable, especially compared to the change in the rest of the ingot. The lower part of the ingot, shown in figure 3.3.3, gives a maximum difference of $4.4 - 1.1 = 3.3$ Ω-cm from the top to the bottom, which is more comparable to the resistivity measurements before thermal donor killing. From this, it is reasonable to conclude that the thermal donors influenced the resistivity to a level comparable to that of the bottom of the ingot.

Figure 3.3.2 also shows much more unstable measurements than those in figure 4.3.2, a trend which is similar to that in the lengthwise plots. The spread

radially the before thermal donor killing results is $1.2 - 1.8 = 0.6$ on $R = 1$, which means that the maximum spread in figure 3.3.2 is about as stable as the lengthwise change in figure 4.3.2. Compared to the lengthwise variation in the rest of the ingot, the measurements after thermal donor killing is be considered stable both radially and lengthwise. Possible explanation of the small unstability may be low concentrations of un-killed thermal donors, or that the sample was contaminated during the heat treatment.

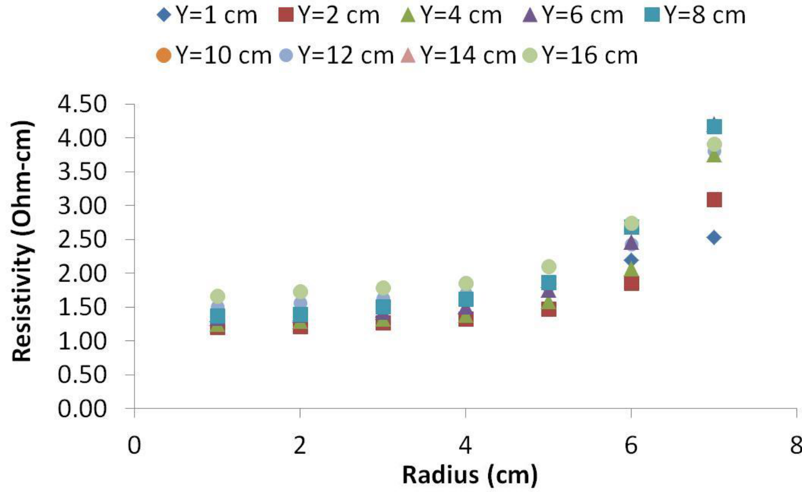

Figure 4.3.2: Resistivity measurements plotted vs. radius for different lengths before TD-killing (37)..

Figure 4.3.3 shows that the resistivity decreases with increasing length. PCD1 and 2 are measurements taken on the outside of the ingot using the PCD tool. FPP and FPP, aTDk are measurements using the FPP before and after thermal donor killing, respectively. FPP measurements after thermal donor killing in the top part is in the same range as the FPP measurements taken on the outside, indicating that the thermal donors concentration is very low at the edge of the ingot. The PCD and FPP results, however, deviate.

Since the PCD is calibrated vs. the FPP (42), and the PCD and FPP gave relatively similar results after 20cm, a calibration error is not assumed to be the main cause. Thus, it is believed that the coil was not in complete contact with the ingot on the top part, due to the relatively bulky surface. The small deviation between the FPP and PCD in the lower part may be caused by the lack of calibration, or lack of complete contact due to the round shape of the ingot, but the difference is so small that it can be neglected.

Figure 1.3.2 shows that increased doping decreases the resistivity. The correlation between the resistivity ρ and the doping level, C, is approximately

$log\rho = -logC$, taken from the figure. Scheil's equation, given in equation 1.4, can thus be rewritten to equation 4.1. Given an end-of-seed resistivity value R_{s0}, equation 4.1 can be used to predict the resistivity for the rest of the ingot. Figure 4.3.4 shows a comparison of the measured resistivity after thermal donor killing and the resistivity expected from the Scheil distribution of the entire ingot.

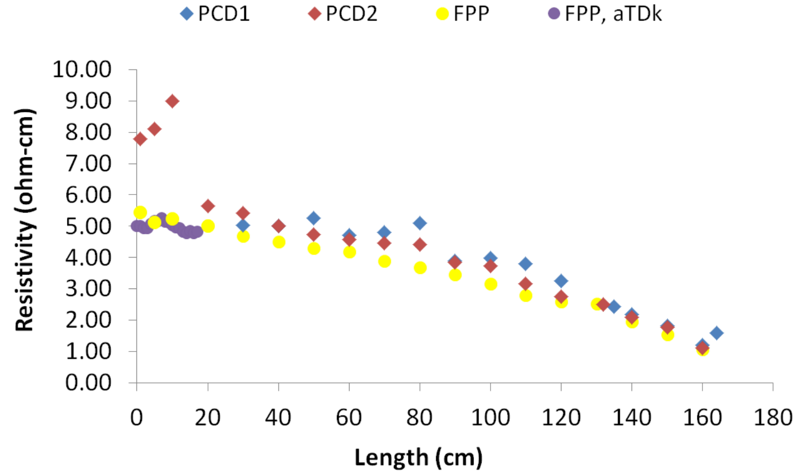

Figure 4.3.3: PCD1 and 2 are measurements taken on the outside of the ingot using the PCD tool. FPP and FPP, aTDk are measurements using the FPP before and after thermal donor killing, respectively. Above 20 there is a large deviation between the FPP and the PCD that is believed to be due to lack of contact, caused by the bulky surface when using the PCD tool.

$$logC = -log\rho = log\rho^{-1} = log(\frac{1}{\rho})$$

$$10^{logC} = 10^{log\frac{1}{\rho}}$$

$$C = \frac{1}{\rho}$$

$$\frac{C_s}{C_{s0}} = \frac{\rho_{s0}}{\rho_s} = (1 - f_s)^{k-1}$$

$$\frac{\rho_s}{\rho_{s0}} = (1 - f_s)^{1-k} \tag{4.1}$$

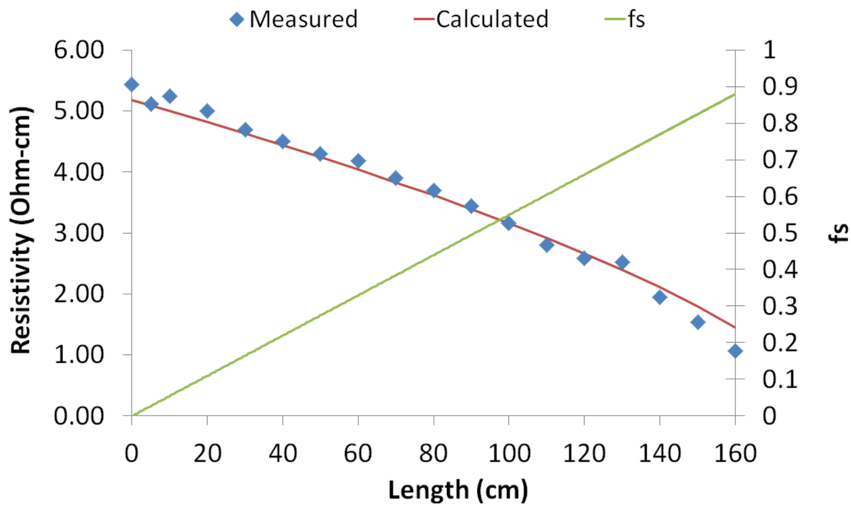

Figure 4.3.4: The measured and calculated resistivity on the outside of the ingot (left axis). The fraction of solid f is on the right axis.

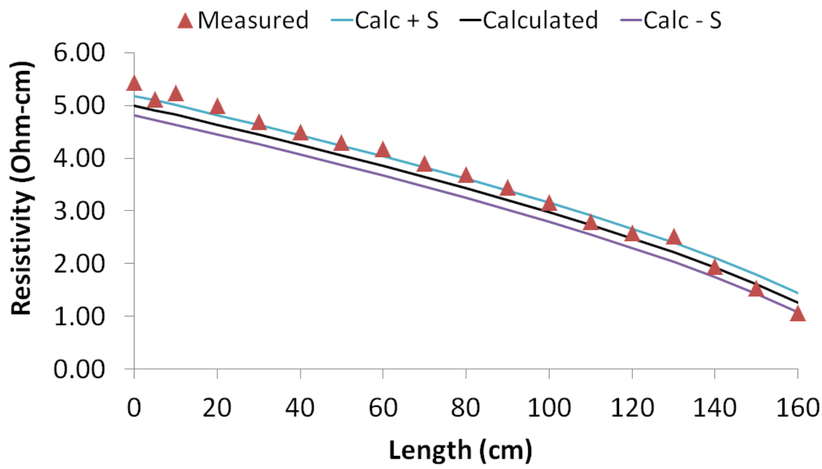

Figure 4.3.5: Resistivity measurements taken on the outside of the ingot, including the standard deviation. .

The standard deviation was calculated from equation 1.25, giving $s = 0.183\Omega$-cm. Figure 4.3.5 shows the resistivity distribution and the standard deviation graphs of the plots.

4.4 Lifetime measurements

Figure 4.4.1 shows the PCD lifetime for the entire ingot (PCD2), including the two radiuses measured on sample 2 in V. Koien (2011) (37) (Inner/Outer, upper part, where Inner was taken at $R = 1-4$ and Outer at $R = 3-7$). PCD1 shows a small increase in lifetime from the first to the second point (1cm and 5cm), then it decreases with increasing length of the entire ingot.

From the measurements on the cross section of the top part, the trend of increased lifetime with increasing radius was believed to be due to the distribution of thermal donors discovered in V. Koien (2011) (37), where the highest concentration was found to be in the center of the ingot. The "Outer, upper part" lifetime was close to PCD1 around 20cm, and the "Inner, upper part" shows the same rapid increase towards the outer measurements, indicating that the concentration of thermal donors is of less significance to the lifetime below 30cm.

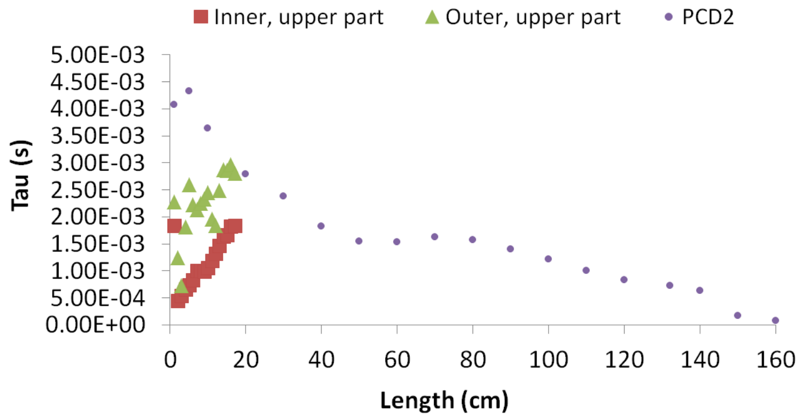

Figure 4.4.1: PCD2 is the lifetime measured on the outside on the entire ingot. The upper part (0-18cm) was measured on two different radiuses (Inner and Outer), which was taken from (37) There is a large difference between the lifetime in the center and PCD1 in the upper parts. In PCD1, the lifetime is decreasing with increasing length, as expected. The cross section measurements are on the other hand increasing with increasing length.

The resistivity on the outside of the ingot is very similar to the measurements after thermal donor killing (see figure 4.3.3), indicating that thermal donors are not main cause of the increase in lifetime at the top of the ingot. At the same time, the influence of thermal donors are dependent on the penetration depth of the lifetime measurements, as the PCD measures the *bulk* lifetime. The radial distribution of thermal donors must therefore be taken into account, which will

be discussed in chapter 4.5.1. On the other hand, the increase from 1 to 5 cm may also be caused by defects. This will be discussed further in chapter4.5.

Figure 3.3.3 shows that the high lifetime in the top part is also associated with deviations in the PCD resistivity measurements. However, the lifetime measurements on transient mode is much less influenced by the lack of complete contact than the quasi steady state mode (42), and the high lifetime measured in this area is thus assumed to give a good indication of what the actual lifetime is.

The curve separating the low and high lifetime sections in the CDI in figure 3.4.2 matches the defect pattern found in both sample 3 and 4, suggesting that there is a difference in lifetime degradation between the interstitial and vacancy rich areas. The lifetime inside the "bubble" seems to be as high as the assumed defect free band surrounding it. The CDI also supports the theory of a vacancy dominated central area inside the plausible H- or L-band found in figure 3.1.11. The change in thermal donor concentration can not be seen on the CDI, which is unexpected. This will be further discussed in section 4.5.

4.5 Doping and impurity effects

In V. Koien (2011) (37) it was assumed that the lifetime degradation in the cross section at the top of the ingot was due to thermal donors. The donor concentration can be calculated by equation 1.9 and 4.6. Using the resistivity measurements from before and after thermal donor killing, the thermal donor concentration can also be calculated. The dopant and thermal donor concentration was calculated in chapter 4.5.1.

Knowing the donor density, the lifetime can be estimated by equation 1.14, assuming no trapping (Auger lifetime). It is also possible to estimate the donor concentration based on the measured lifetime. If the lifetime on the other hand is trap dominated, the lifetime can be estimated by equation 1.15, if the trap density is known (SRH lifetime). Knowing the lifetime and the dopant concentration, the trap density can be estimated. The Auger and SRH lifetime was estimated in section 4.5.2 and 4.5.3, respectively, to confirm or dis-confirm the assumption of thermal donors solely being responsible for the lifetime degradation.

4.5.1 Dopant and thermal donor calculations

Assuming $T = 300$K, equation 1.9 can be rewritten to equation 4.2 for calculations assuming no thermal donors, and equation 1.13 if thermal donors are present.

$$\mu(N_D) = 88 + \frac{7.4 * 10^8 * 300^{-2.33}}{1 + \frac{0.88 N_D}{1.26 * 10^{17}}} \tag{4.2}$$

$$\mu(N_D + 2[TD]) = 88 + \frac{7.4 * 10^8 * 300^{-2.33}}{1 + \frac{0.88(N_D + 2[TD])}{1.26 * 10^{17}}} \tag{4.3}$$

N_D was derived from 1.10 and 4.2, solving for $\mu(N_D)$. The concentration of N_D could thus be directly calculated by equation 4.6.

$$\mu(N_D) = \mu(N_D)$$

$$\frac{1}{N_D \varrho q} = 88 + \frac{7.4 * 10^8 * 300^{-2.33}}{1 + \frac{0.88 N_D}{1.26 * 10^{17}}}$$

Simplifications:

a = 88, b = $7.4 * 10^8 * 300^{-2.33} = 1252$, c = $1.26 * 10^{17}$, d = 0.88, x = N_D

$$\frac{1}{\mathrm{x}\rho q} = a + \frac{b}{1 + \frac{dx}{c}} \tag{4.4}$$

$$\frac{1}{\rho q}(1 + \frac{dx}{c}) = ax(1 + \frac{dx}{c}) + bx$$

$$\frac{1}{\rho q} + \frac{dx}{\rho qc} = ax + \frac{ad}{c}x^2 + bx$$

$$\frac{ad}{c}x^2 + (a + b - \frac{d}{\rho qc})x - \frac{1}{\rho q} = 0 \tag{4.5}$$

$$N_D = x = \frac{-(a + b - \frac{d}{\rho qc}) + \sqrt{(a + b - \frac{d}{\rho qc})^2 + 4\frac{ad}{\rho qc}}}{2\frac{ad}{c}} \tag{4.6}$$

Negative values are invalid. Knowing N_D, [TD] could be derived from equation 1.12 and 1.13 similar to the derivation of N_D. $(N_D + 2[TD])$ was simplified to $(x+2y)$, where $x = N_D$ and $y = [TD]$. Effectively, this corresponds to replacing x with $(x + 2y)$ in equation 4.5, as shown in equation 4.7. The concentration of [TD] for each position could then be calculated directly from equation 4.8.

$$\frac{ad}{c}(x + 2y)^2 + (a + b - \frac{d}{\rho qc})(x + 2y) - \frac{1}{\rho q} = 0 \tag{4.7}$$

Simplifications:

$A = \frac{ad}{c} = 6.15 * 10^{-16}$, $B = a + b - \frac{d}{\rho qc} = 1.33 * 10^3$, $C = -\frac{1}{\rho q} = -1.34 * 10^{18}$

$$A(x + 2y)^2 + B(x + 2y) + C = 0$$

$$Ax^2 + 4Axy + 4Ay^2 + Bx + 2By + C = 0$$

$$4Ay^2 + (4Ax + 2B)y + Ax^2 + Bx + C = 0$$

$$4A[TD]^2 + (4AN_D + 2B)[TD] + AN_D^2 + BN_D + C = 0$$

$$[TD] = \frac{-(4AN_D + 2B) + \sqrt{(4AN_D + 2B)^2 - 16A(AN_D^2 + BN_D + C)}}{8A} \quad (4.8)$$

The resistivity measurements were done on sample 1 before and after TD-killing, where the before-measurements were taken from (37). They were used to calculate the donor (N_D) and the thermal donor ([TD]) concentration. For an example of $\rho = 4.65$, equation 4.6 gave $N_D = 1.01 * 10^{15} cm^{-3}$, and correspondingly $[TD] = 9.5842 * 10^{14} cm^{-3}$ from equation 4.8. N_D and $[TD]$ was calculated for each ρ from the different positions on the sample. Figure 4.5.1 and 4.5.2 shows the thermal donor distribution lengthwise and radially, respectively.

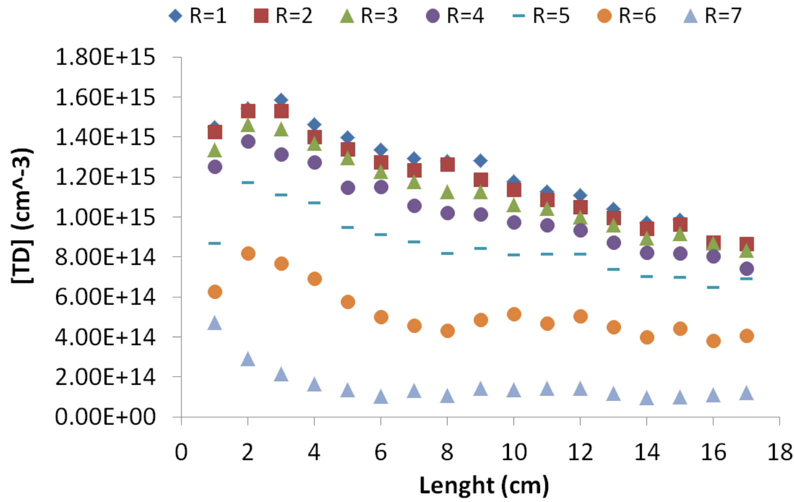

Figure 4.5.1: TD-map for different radiuses plotted vs. length. The TD concentration is decreasing steadily after $Y = 3$cm. Before this the concentration increases. The difference in radius is small from $R = 1-4$, and vastly increasing from $R = 5$ and out.

The concentration is, as expected from the resistivity distribution, highest in the center of the ingot, as the resistivity is the lowest here. The concentration close to the edge is very low compared to the center. Even the highest concentration on $R = 7$ is lower than the lowest concentration from $R = 1 - 5$. From R=5 and outwards, the concentration drops, whereas farther in than this the decrease

with increasing radius is smaller. The decrease lengthwise is largest in the center of the ingot, and the concentration closer to the edge is more stable, especially from around $Y = 6$cm for $R = 6$ and $Y = 4$cm for $R = 7$.

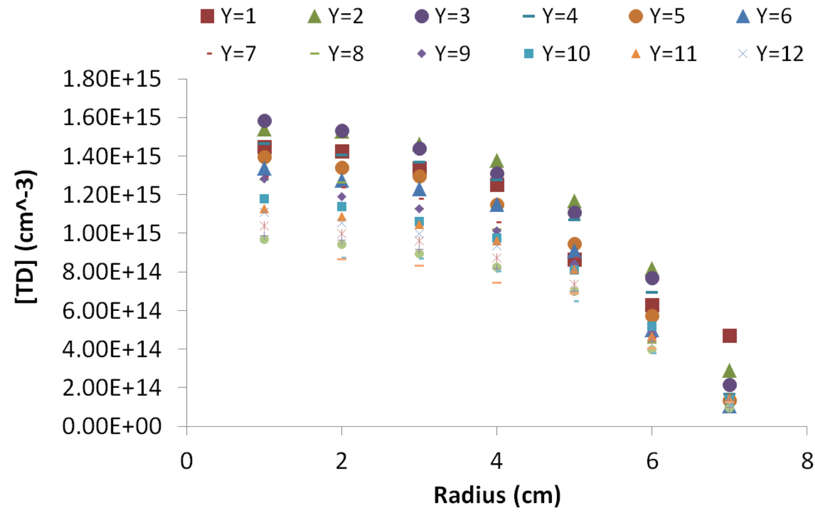

Figure 4.5.2: TD-map for different lengths plotted vs. radius. Between $R = 1 - 4$, there is only a slight decrease in concentration, but further out than this, the change steepens. For the lengths before $R = 4$, the spread between the points are much more spread than the radiuses closer to the edge.

The dopant density in figure 4.5.3 was calculated for the outside of the ingot body using equation 4.6, along with the FPP resistivity measurements from the outside of the ingot, shown in figure 3.3.3. The increasing donor concentration corresponds to what is expected from Scheil's equation (equation 1.4), as it is similar to the curve illustrated in figure 1.3.1.

Figure 4.5.4 shows the donor distribution before and after thermal donor killing for two different radiuses ($R = 1$ and $R = 7$), compared the measurements taken on the outside of the ingot. The plots for both radiuses *after* thermal donor killing correlates very well with the measurements taken on the outside of the ingot, as expected from the resistivity measurements.

The results from *before* the thermal donor killing shows that the concentration of thermal donors in the center of the ingot was as high as the concentration found close to the tail. Assuming no trapping, the lifetime should be the same on the top and on the bottom of the ingot. Figure 4.4.1 indicates that thermal donors are the main cause of lifetime reduction in the top part.

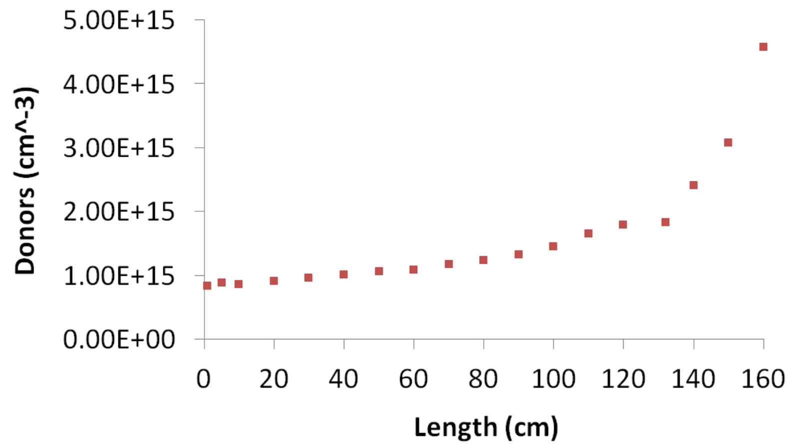

Figure 4.5.3: The dopant density was calculated from equation 4.6, using the FPP resistivity measurements taken from the outside of the ingot, as shown in figure 3.3.3. The calculations give an increasing amount of donors towards the bottom of the ingot, as expected from Scheil's equation.

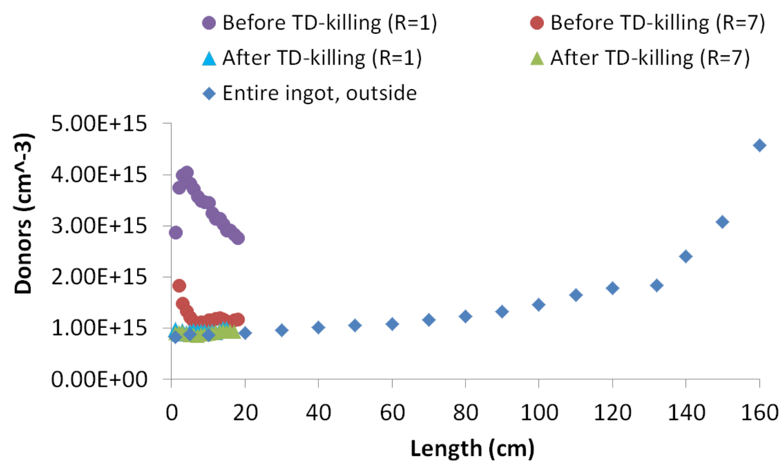

Figure 4.5.4: Dopant density for the entire ingot. The two different radiuses on the top part is from sample 1, which was measured on both before and after TD-killing. Thermal donors were clearly present here. After TD-killing, the donor concentration in the top part correlates to the lower parts of the ingot, as expected.

Although the thermal donors do not seem to disappear until after 40cm, the lifetime measurements in figure 4.4.1 indicate that after 30cm the concentration is too low to influence the lifetime. Cross section investigations of the area 20-40cm must be done to acquire knowledge of the real dopant an lifetime situation here. The lifetime measurements will be further discussed in section 4.5.2 and 4.5.3.

The total donor concentration was only slightly higher than the phosphorous concentration at $R = 7$, except from 5cm and up, where the difference is increasing towards the top of the ingot. Given that the penetration depth is important for how much the thermal donors influence the lifetime, the thermal donor distribution for $R = 7$ indicate that thermal donors may influence the lifetime above 5cm in figure 4.4.1, as the concentration is higher here than farther down.

The donor density was also calculated by equation 1.6, given by the symbol n_D. For an example of $\rho = 4.65$, n_D was calculated to:

$$Z = \frac{A_0 + A_1 log\ 4.65 + A_2(log\ 4.65)^2 + A_3(log\ 4.65)^3}{1 + B_1 log\ 4.65 + B_2(log\ 4.65)^2 + B_3(log\ 4.65)^3} = -3.139$$

$$n_D = \frac{6.242 * 10^8}{4.65} * 10^{-3.139} = 9.75 * 10^{14} cm^{-3}$$

The same calculation from equation 4.6 gave $N_D = 1.01 * 10^{15} cm^{-3}$. The difference between the 2 answers is $\approx 3.4 * 10^{17} cm^{-3}$. Figure 4.5.5 shows how n_D compares to N_D and [TD] from the equations4.6 and 4.8, in a lengthwise perspective. Figure 4.5.6 shows the same in a radial perspective. n_D(bTD-k) indicates the density before thermal donor killing, and n_D(aTD-k) indicates after thermal donor killing.

The deviation between N_D and n_D(aTD-k) is relatively small in both figure 4.5.5 and 4.5.6. n_D(bTD-k) also corresponds well with the sum of $N_D + 2[TD]$, calculated from equation 4.6 and 4.8, respectively. This is as expected since n_D is supposed to be equal to $N_D + 2[TD]$ before TD-killing, thus indicating that the calculation of [TD] is correct. If there were errors in the calculation of [TD], n_D and $N_D + 2[TD]$.

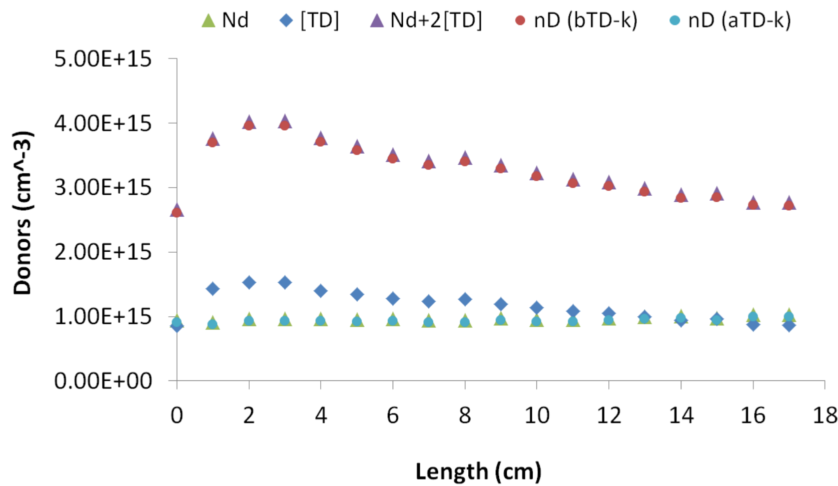

Figure 4.5.5: Donors vs. length, comparison of n_D from equation 1.6 and N_D from 4.6 for calculating donors. n_D(bTD-k) illustrates the density before thermal donor killing, and n_D(aTD-k) illustrates after thermal donor killing. The deviation between between N_D and n_D (aTD-k) is relatively small. n_D(bTD-k) also correspond well with the sum of $N_D+2[TD]$, indicating that the calculation of [TD] is correct.

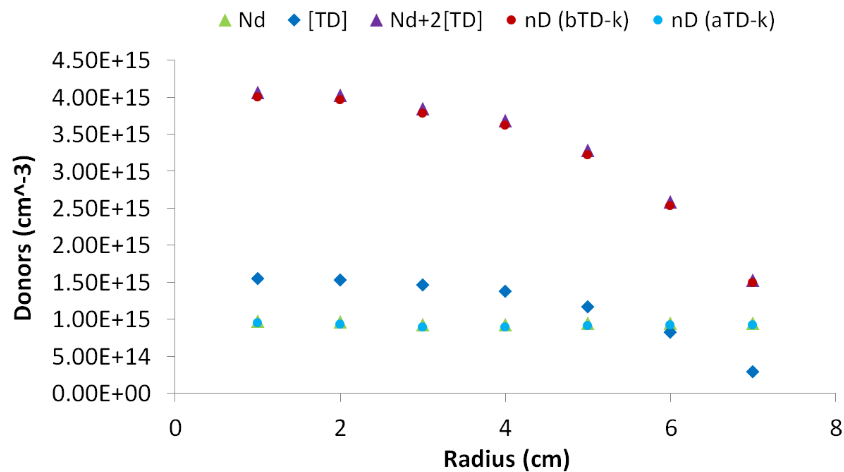

Figure 4.5.6: Donors vs. radius, comparison of equation 1.6 and 4.6 for calculating thermal donors. The deviation using the two different equations are small, also in a radial perspective.

The concentration of the thermal donors seems to be up to about 1.5 times the phosphorous concentration at the highest. This gives about 3 times the doping effect compared the measured amount of phosphorous, as thermal donors are double donors.

4.5.2 Lifetime estimations assuming Auger recombination

Assuming only Auger recombination, the doping level n_0 can be calculated by equation 1.14, which can be rewritten to equation 4.9. p_0 is very small in n-doped Si, hence it can be neglected. $C_n = 2.8 * 10^{-31}$ and $C_p = 10^{-31}$ for Si at 300K.

$$\tau_{Aug} = \frac{1}{C_p(p_0{+}\Delta \mathrm{n})^2{+}C_n(n_0{+}\Delta \mathrm{n})^2} \tag{4.9}$$

The dopant concentration can then be estimated by converting equation 4.9 to equation 4.10.

$$n_0 = \sqrt{\frac{\frac{1}{\tau_{Aug}} - C_{p*}\Delta n^2}{C_n}} - \Delta n \tag{4.10}$$

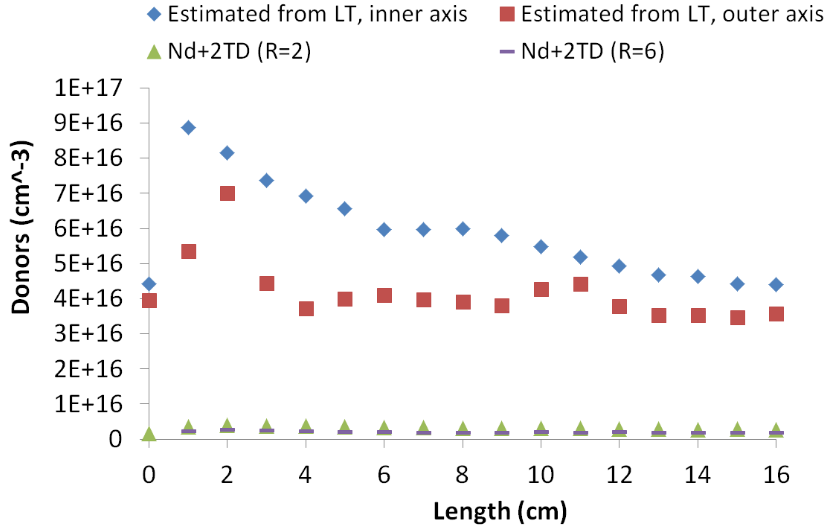

Figure 4.5.7: Donors estimated from the lifetime measurements (assuming only Auger recombination) compared with the donor densities from the resistivity measurements (FPP). Plotted vs. length.

With a lifetime of $\tau = 1.84 * 10^{-3}$ s at an injection level $\Delta n = 5 * 10^{14}$, n_0 was calculated to:

$$n_0 = \sqrt{\frac{\frac{1}{1.84*10^{-3}} - 10^{-31}*(5*10^{14})^2}{2.8*10^{-31}}} - 5*10^{14} = 4.36*10^{16}cm^{-3}$$

Figure 4.5.7 shows how the donor concentration, including the thermal donors, changes with length from the entire ingot. Figure 4.5.9 corresponds to 4.4.1, but also includes the estimated lifetime from equation 4.9, based on the dopant concentration.

On figure 4.5.7, both the calculated donor concentration and the estimated concentration from equation 1.14, assuming only Auger recombination, is plotted. The figure shows that the donor levels are much smaller than what was expected from the lifetime measurements if no trapping happens (no SRH-recombination). Still, even with the thermal donors, the total donor effect isn't nearly as large as expected.

From figure 4.5.9 it is reasonable to believe that trapping is a plausible reason for the low measured lifetime compared to the estimated, since radiation recombination does not happen in Si. Thermal donors, like donors, also reduce the lifetime, but are only expected to exist in the upper parts of the ingot. Thus, the lifetime on the lower parts below 30cm is not believed to be significantly influenced by thermal donors, as assumed in 4.4. Since there is no relative reduction between estimated and measured lifetime with increasing length, trapping is believed to be the main cause of the difference between the two.

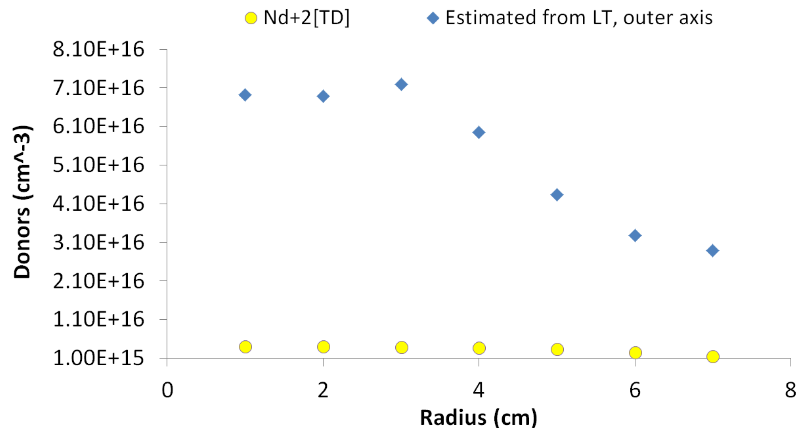

Figure 4.5.8: Donors estimated from the lifetime measurements (assuming only Auger recombination) compared with the donor densities from the resistivity measurements (FPP). Plotted vs. radius.

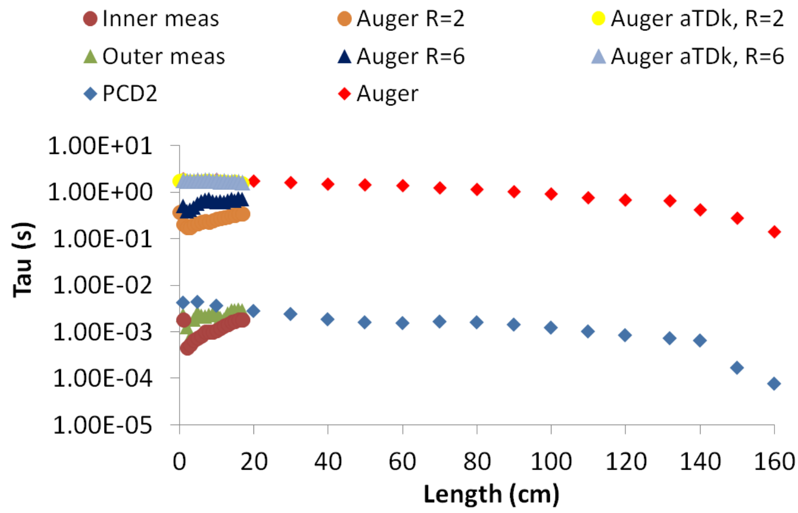

Figure 4.5.9: This figure corresponds to figure4.4.1, here compared with the estimated lifetimes based on having only Auger recombination. Auger lifetime was estimated for the body and the cross section at R=2 and R=6 before and after thermal donor killing (aTDk).

4.5.3 Lifetime estimations assuming SRH recombination

Since the estimated lifetime is based on the Auger lifetime equation, this can mathematically be described as: $\tau_{Aug} = \tau_{est}$. The difference between the measured and the estimated lifetime in figure 4.5.9 can thus be expressed as:

$$\tau_{est} - \tau_{meas} \approx \tau_{Aug} - \tau_{meas} \tag{4.11}$$

Since the measured lifetime consists of the components given in equation 1.3, and radiative recombination is unusual in Si, the equation can be expressed as:

$$\tau_{Aug} - \tau_{meas} \approx \tau_{Aug} - \frac{1}{\tau_{Aug}^{-1} + \tau_{SRH}^{-1}} \tag{4.12}$$

If τ_{Aug} is large compared to τ_{SRH}, the equation can be rewritten to:

$$\tau_{Aug} - \tau_{meas} \approx \tau_{Aug} - \tau_{SRH} \tag{4.13}$$

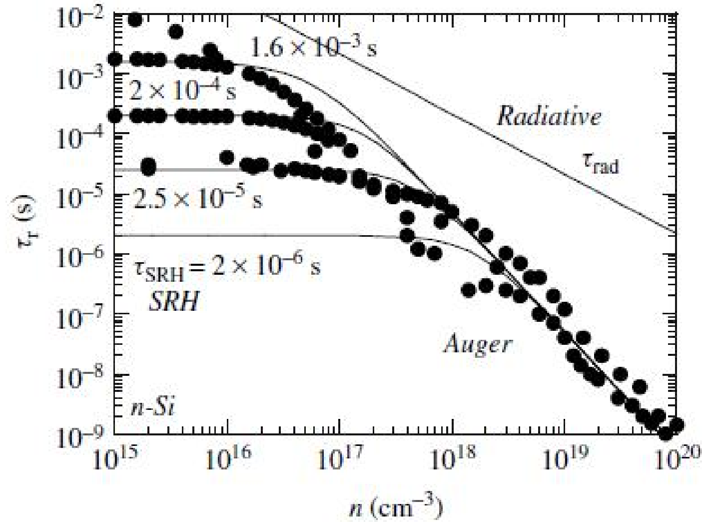

Figure 4.5.10: The graph shows a plot of lifetime vs. majority carrier concentration for n-type Si (11).

Removing the τ_{Aug} on both sides gives $\tau_{meas} \approx \tau_{SRH}$. In other words, since the estimated or the auger lifetime is so high compared to the measured lifetime, equation 4.13 is valid, meaning that the lifetime is trap dominated. This is consistent with figure 1.3.3, also shown in figure 4.5.10, for the n values ($n = n_0 + \Delta n \approx 10^{15} cm^{-3}$) and lifetime ($\tau_{meas} \approx 10^{-3} s$) measured in this ingot, which corresponds to the SRH dominated lifetime.

The highest level of donors measured was around $4 * 10^{15} cm^{-3}$ at around Y = 3cm, and the lifetime up to $4.3 * 10^{-3}$s at Y = 17 cm. On figure 4.5.10, this corresponds to the SRH-dominated area. After thermal donor killing, the donor levels were on the first 20cm around $1 * 10^{15} cm^{-3}$, means that the major recombination mechanism still should be SRH-dominated.

4.5.3.1 Example with iron traps

Traps can be categorized into two types: metallic and non-metallic. Metallic traps are expected to be Scheil distributed similarly to the example in figure 1.3.1. Iron is a metal that can cause traps in silicon (12), and is used as an example of metallic trapping. SRH-lifetime was used to calculate the density of electrically active iron, to see if iron could fit as a cause of the lifetime degradation.

The trap level for iron in Si is $E_T = E_V + 0.38eV$ (14). The capture cross sections are $\sigma_n = 5 * 10^{-14} cm^2$ and $\sigma_p = 7 * 10^{-17} cm^2$. $E_i = 0.02eV$ for Si (12), and $n_i = 1.08 * 10^{10} cm^{-3}$for Si at 300K (43). m_{th} is equal to $m_{tc} = 0.28 * m_0$ for the conduction band, and equal to $m_{tv} = 0.41 * m_0$ for the valence band, where m_0 is the electronic rest mass = $9.10938188 * 10^{-31}$ kg (41). Since the Boltzmann constant is in Joule, it has to be multiplied with $6.24150974 * 10^{18}$ eV/J.

$$n_1 = 1.08 * 10^{10} exp(\frac{0.38 - 0.02}{1.38 * 10^{-23} * 300 * 6.24 * 10^{18}}) = 1.21 * 10^{16} cm^{-3} \quad (4.14)$$

$$p_1 = 1.08 * 10^{10} exp(-\frac{0.38 - 0.02}{1.38 * 10^{-23} * 300 * 6.24 * 10^{18}}) = 9.68 * 10^{3} cm^{-3} \quad (4.15)$$

$$\upsilon_{tc} = \sqrt{8 * 0.38 * 10^{-23} * 300/\pi * 0.28 * 9.11 * 10^{-31}} = 2.03 * 10^{7} cm/s \quad (4.16)$$

$$\upsilon_{tv} = \sqrt{8 * 0.38 * 10^{-23} * 300/\pi * 0.41 * 9.11 * 10^{-31}} = 1.68 * 10^{7} cm/s \quad (4.17)$$

From the calculations shown in equation 4.18 and 4.19, the trap or iron density N_T can be derived from equation 1.15, as shown in equation 4.21.

$$\tau_n = \frac{1}{5*10^{-14}*2.75*10^{14}*N_T} \quad (4.18)$$

$$\tau_p = \frac{1}{7*10^{-17}*2.28*10^{14}*N_T} \quad (4.19)$$

Simplifications:

$A = 5 * 10^{-14} * 2.75 * 10^{14}$, $B = 7 * 10^{-17} * 2.28 * 10^{14}$

$$\tau_{SRH} = \frac{\frac{1}{AN_T}(n_0 + n_1 + \Delta n) + \frac{1}{BN_T}(p_0 + p_1 + \Delta p)}{p_0 + n_0 + \Delta n}$$

$$\tau_{SRH} = \frac{(\frac{1}{A}(n_0 + n_1 + \Delta n) + \frac{1}{B}(p_0 + p_1 + \Delta p))}{N_T(p_0 + n_0 + \Delta n)} \quad (4.20)$$

$$N_T = \frac{(\frac{1}{A}(n_0 + n_1 + \Delta n) + \frac{1}{B}(p_0 + p_1 + \Delta p))}{\tau_{SRH}(p_0 + n_0 + \Delta n)} \quad (4.21)$$

The relationship between n and p i shown in equation 4.22, where n_i is the intrinsic concentration of electrons (12). The value of Δp can be derived as shown in equation 4.23, assuming that $p_0 << n$ and therefore insignificant. Equation 4.21 can thus be rewritten to equation 4.24.

$$pn = n_i^2 \quad (4.22)$$

$$\Delta p(n_0 + \Delta n) = n_i^2$$

$$\Delta p = \frac{n_i^2}{n_0 + \Delta n} \quad (4.23)$$

$$N_T = \frac{(\frac{1}{A}(n_0 + n_1 + \Delta n) + \frac{1}{B}(p_1 + \frac{n_i^2}{n_0+\Delta n}))}{\tau_{SRH}(n_0 + \Delta n)} \tag{4.24}$$

The iron trap density was estimated for the entire ingot based on the measured lifetime, assuming that the highest measured lifetime (at $Y = 5$, see figure 4.4.1) is the highest lifetime achievable, and that iron is the only cause of the traps. For a doping level of $n_0 = 8.83 * 10^{14}$ and a measured lifetime of $4.33 * 10^{-3}$s, the iron trap density N_T at $Y = 5$cm was calculated to:

$$N_T = \frac{(\frac{1}{A}(n_0 + n_1 + \Delta n) + \frac{1}{B}(p_1 + \frac{n_i^2}{n_0+\Delta n}))}{\tau_{SRH}(n_0 + \Delta n)} = 2.21 * 10^9 cm^{-3}$$

Figure 4.5.11 shows the iron density $N_{T(Fe)}$ that is required to cause the the gap between the estimated and measured lifetime on figure 4.5.9.

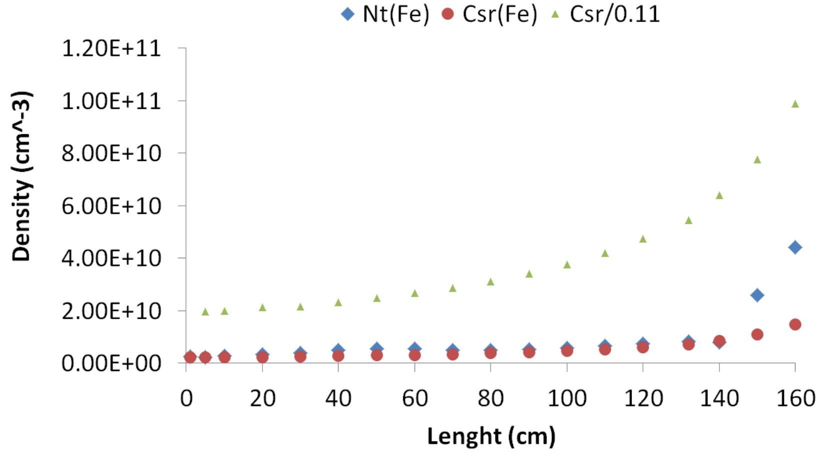

Figure 4.5.11: $N_{T(Fe)}$ is the iron trap density required to decrease the lifetime equal to the difference in the measured and calculated in figure 4.5.9. The iron concentration is also predicted by Scheil's equation, given by $C_{sr(Fe)}$ based on the value of $N_{T(Fe)}$ at 5cm. Both curves show an increase towards the end of the ingot, but deviate from each other after 140cm. $C_{sr}/0.11$ is the real iron density, as only 11% of the interstitial iron is electrically effective (22).

The concentration of iron predicted by Scheil's equation 1.4 is also plotted, given the starting concentration of $C_{s0} = N_{T(Fe,Y=5)} = 2.21 * 10^9 cm^{-3}$, and using relative f_s; $f_{sr(Y)} = f_{s(Y)} - f_{s(Y=5)}$, thus creating a relative C_s; $C_{sr(Fe)}$

given in equation 4.25. For iron, $k = 5 * 10^{-6}$(22). However, not all the iron is electrically active, and a relationship of $N_T = 0.11 * C_s$ for iron is stated by Coletti et. al., where the total iron density is described by Csr/0.11 in figure 4.5.11. Csr(Fe) describes the estimated concentration of electrically active iron.

$$C_{sr(Fe,Y)} = 2.21 * 10^9 (1 - f_{sr(Y)})^{(5*10^{-6}-1)} \tag{4.25}$$

N_T and C_{sr} seem to coincide relatively good with each other up to 140cm, which indicates that the trapping my be Scheil distributed. On the other hand, the fact that N_T is higher than C_{sr} on some places indicates that there are other non-metallic traps present in addition. As an example, the deviation after 140cm may be caused by structure loss defects, which could be interpreted from the disappearance of the nodes of the ingot in the tail part (44).

Given the Scheil distribution of electrically active iron $C_{sr(Fe,Y)}$, it was possible to calculate an estimated lifetime after thermal donor killing from the donor concentration measured on the outside of the ingot, assuming only iron traps, shown in figure 4.5.12. For $n_0 = 8.83 * 10^{14}$, at $Y = 5$cm (at the highest measured lifetime), the SRH lifetime was calculated to:

$$\tau_{SRH(Y)} = \frac{(\frac{1}{A}(n_0 + n_1 + \Delta n) + \frac{1}{B}(p_1 + \frac{n_i^2}{n_0 + \Delta n}))}{C_{sr(Fe,Y)}(n_0 + \Delta n)} = 4.33 * 10^{-3} s$$

Summary of assumptions made for the calculation of SRH lifetime on the outside of the ingot:

- The highest measured lifetime (which is at $Y = 5$) is due to only iron traps, assuming that this must be the highest iron concentration allowed in the ingot, as the estimated lifetime cannot be lower than the measured lifetime.

- A relative f_s is used, $f_{sr(Y)} = f_{s(Y)} - f_{s(Y=5)}$, making $f_{sr} = 0$ at $Y = 5$, in other words “pretending” that $Y = 5$ is at the top of the ingot and f_{sr} is the relative fraction of solid from this point on.

- The relative f_{sr} produces a relative C_{sr} using equation 4.25.

- The estimated SRH lifetime is calculate using equation 4.20, where C_{sr} is used instead of N_T, and thus is based on the *expected* Scheil distribution of iron (with $Y = 5$ as the base point).

For a fixed contaminant like iron, the only parameters that changes in equation 4.20 is n_0 and N_T (or C_{sr} in this case). In figure 4.5.12, both the measured, estimated, and two variations of the estimated lifetime was plotted. "Estimated, Csr = const" is when C_{sr} is kept constant, and "Estimated, n_0 = const" when n_0 is kept constant. The plot from when n_0 remains unchanged, in other words when only C_{sr} changes, is much more similar to both the estimated and measured plots. This shows that C_{sr} has the largest influence on the lifetime.

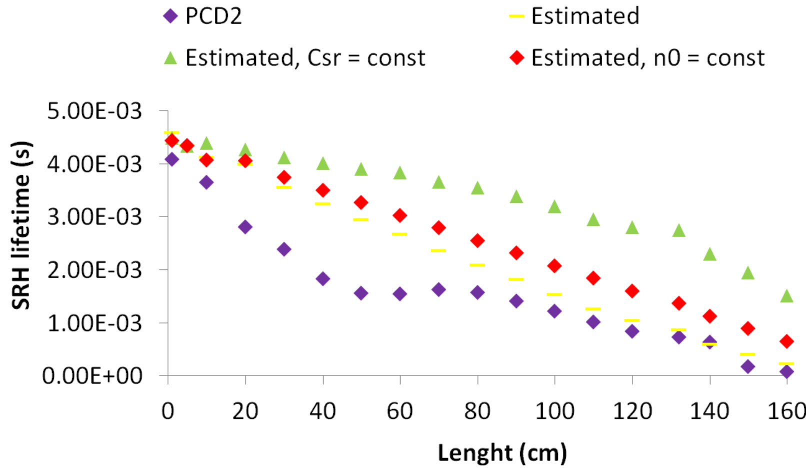

Figure 4.5.12: The measured lifetime, PCD2, compared with the estimated lifetime, plus the estimated lifetime where either C_{sr} or n_0 is kept constant. C_{sr} seems to influence the lifetime more than n_0, but the influence of n_0 becomes more important to the lifetime at the bottom of the ingot, as the donor concentration increases rapidly here. The difference between the estimated and measured lifetime is believed to be caused by non-metallic traps.

Another important issue is the difference between C_{sr} and N_T, indicating that there are other, non-metallic traps present, as a metallic trap would have a curve that is more straight, or bent slightly in the opposite direction, due to the Scheil distribution. It is thus reasonable to assume that N_T changes according to equation 4.26, where X is the concentration of non-metallic traps with an unknown efficiency, and C_s is the Scheil concentration of the metal.

$$N_T = C_s + X \tag{4.26}$$

The graph in figure 4.5.11 show a large deviation between C_{sr} and N_T after 140cm, but this does seem not induce a significant difference between the estimated and measured lifetime on figure 4.5.12. The reason seems to be that

the change in n_o becomes more important in the equation, as the gap between "Estimated, Csr = const" and "Estimated, n_0 = const" decreases again, after being increased between 5-130cm. Figure 4.5.3 shows that from 140cm, the dopant concentration curve is very steep.

Higher up in the ingot, n_0 is much more stable. The difference between N_T to C_{sr}, which corresponds to the difference between the measured and estimated lifetime, respectively, will thus have a larger influence on the lifetime here. This can be seen from the small deviation between C_{sr} and N_T from 20-140cm on figure 4.5.11, which seems to have a large influence on the deviation between the estimated and measured lifetime. Above 20cm, N_T and C_{sr} are almost overlapping on figure 4.5.11, but on figure 4.5.12, even the slightest difference between N_T and C_{sr} causes a difference in lifetime here. This indicates that the concentration of non-metallic trap, X, has a large influence on the lifetime here.

In the case of other metallic traps, the two factors that would change is the k-value, which influences C_s, and n_1, which is constant for the same material. n_1 does not influence the shape of the graph in figure 4.5.12, as the estimated lifetime is based on the value at $Y = 5$. A higher k-value would lead to a lower C_s with increasing length, and thus increasing X with increasing length, causing an increasingly large difference between the measured and estimated lifetime.

This can be seen from equation 1.4. However, the straight shape of the otherwise decreasing curve remains. The more curvy nature of the measured lifetime is thus assumed to be caused by a relatively high value of X. Hence, a metal contaminant which introduces trap levels is a plausible reason for the lowering from the estimated Auger lifetime to the estimated SRH-lifetime, but the presence of non-metallic traps seems relatively certain.

Figure 4.5.13 shows the measured and estimated lifetime, plus the measured and estimated lifetime for the cross section of the top part of the ingot, calculated both with and without the thermal donors. All the estimated values were, however, based on the same C_{sr} values from equation 4.25, assuming only iron traps.

Assumptions for the SRH lifetime calculations on the cross section:

- N_T is calculated based on the total donor concentration, including the thermal donors. Separate N_T values are calculated for the inner and outer plots, to investigate if N_T varies with radius.
- An individualC_{sr} is calculated for both radiuses based on the individual N_T values. The base point is still at $Y = 5$, since if N_T is caused by only iron, the iron concentration should be relatively equal throughout the cross section, and should thus give equal lifetimes for all radiuses, given an equal donor concentration.

- The SRH lifetime is calculated for the individual radius with it's individual C_{sr} using the total donor concentration, as SRH lifetime is calculated based on the "thermal equilibrium value, n_0" (28), making it applicable to doping due to thermal donors, as well as normal phosphorous doping.

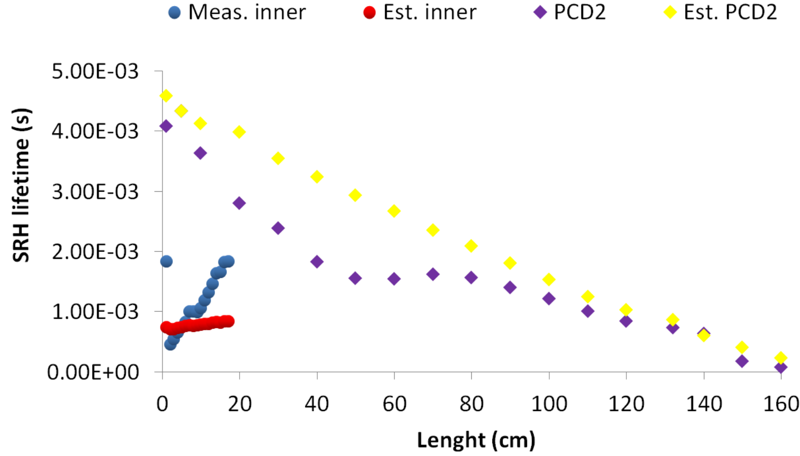

Figure 4.5.13: "PCD2" is the measured lifetime at the outside of the ingot. "Est." indicates that the plot is estimated, and "Meas." that it is measured. Est. inner is lower than Meas. inner, which is not possible. Hence all the estimated plots need to be lifted, forcing the estimated lifetime in the cross section to be higher than the measured. "Est. Inner" shows that event the fast decrease in total donor concentration is large enough to steepen the curve to the level of "Meas, inner".

Est. inner is lower than the measured lifetime (Meas. inner) which is not possible. Hence all the estimated plots need to be lifted, forcing the estimated lifetime in the cross section to be higher than the measured. This causes a gap between "PCD2" and "Est. PCD2", which indicates that iron is *not* the only source of traps in $Y = 5$. The heightening of the estimated lifetime also means that C_{sr} in figure 4.5.11 must be lowered by at least:

$$\Delta C_{sr(Fe,Y)} = \frac{(\frac{1}{A}(n_0 + n_1 + \Delta n) + \frac{1}{B}(p_1 + \frac{n_i^2}{n_0+\Delta n}))}{\Delta\tau_{SRH}(n_0 + \Delta n)}$$

where $\Delta\tau_{SRH}$ is the heightening lifetime and $C_{sr(Fe,Y)} - \Delta C_{sr(Fe,Y)}$ is the corrected maximum iron trap density. Since the lifetime seems to be unaffected

by TDs after 30cm, the estimated plots in figure 4.5.14 were heightened by $\Delta\tau_{SRH}$ =("PCD2", $Y = 30$) - ("Est. inner", $Y = 5$) $= 1.63 * 10^3$. Figure 4.5.15 shows the plot for the outer radius of the lifetime measurements in the cross section compared with the measurements taken on the outside of the ingot. The estimated plots in figure 4.5.14 were also heightened by $\Delta\tau_{SRH}$.

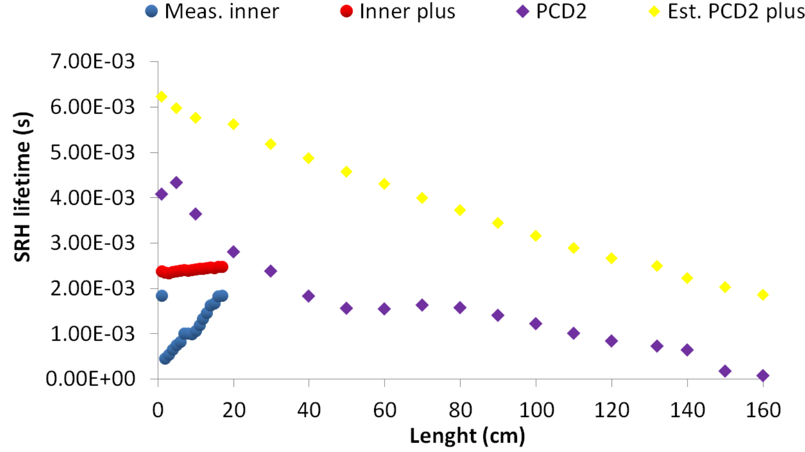

Figure 4.5.14: Corrected plot of figure 4.5.13, heightened by the height difference between "Est. inner" at $Y = 5$ and "PCD2" at $Y = 30$. "Inner plus" is the estimated plot for the "inner" radius including the height correction. The gap between "PCD2 plus" and "Inner plus" is believed to be caused by thermal donors and metallic traps such as iron, while the gap between the estimated and measured inner values is believed to be due to non-metallic traps, X.

The estimated lifetime in the cross section does not mach the measured lifetime for the given concentration of thermal donors in both figure 4.5.14 and 4.5.15. This is an indication that thermal donors are not the only cause of the lifetime reduction. "Est. Inner" and "Est. Outer" on figure 4.5.14 and 4.5.15, respectively, both show that despite the rapid decrease in total donor concentration from top to bottom of the top part samples, this is not sufficient to steepen the curve to their respective measured values in the cross section. It is also noticeable that the lifetime in the cross section, when extrapolating the curve, seem to even out with the lifetime on the outside of the ingot at around 20cm. The thermal donor density, on the other hand, seems to last until at least 40cm, indicating that the thermal donor concentration after 20cm are of less importance to the lifetime.

The poor fit between the estimated and measured lifetime in the cross section in figure 4.5.14 and 4.5.15, indicates that the concentration of non-metallic traps,

X, is even higher in the center parts, and that these traps are an important contributor to the lowering of the lifetime in the center. The cause of non-metallic traps will be further discussed in 4.5.3.2.

Figure 4.5.16 shows the radial change in lifetime for the estimated and measured values on sample 2 (from (37)). The measured lifetime values here were taken with the length side of the coil pointing in the length direction of the ingot, giving a better radial solution of the measurements. The estimated cross section lifetimes “Est. inner” and “-outer” were calculated using the donor concentration averaged over 4cm in length to equal the length of the PCD coil, as the concentration of thermal donors changes with radius.

The estimated values were also heightened equally to those in figure 4.5.14. Est. aTDk corresponds to the estimated lifetime after thermal donor killing, and should be representative for the entire cross section down to 18cm, as the resistivity measurements in figure 3.3.1 and 3.3.2 both show that the donor concentration here is very stable.

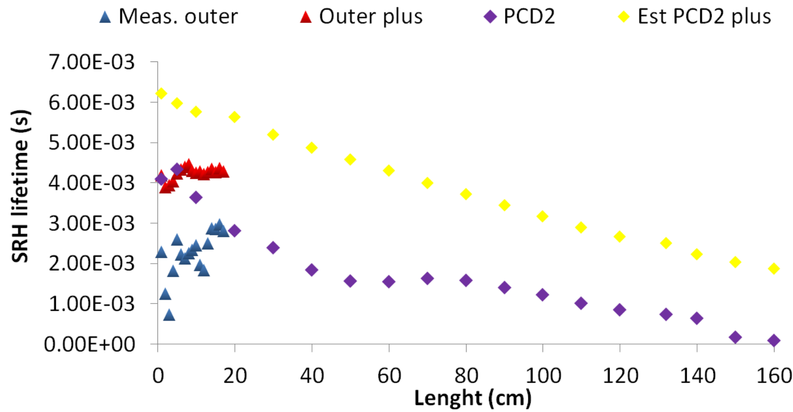

Figure 4.5.15: The corrected values for the estimated and measured values for the “Outer” radius. Since PCD2 doesn’t match Est. PCD2 plus, non-metallic traps must be present to cause the gap between the two.

Similar to what was found in figure 4.5.14 and 4.5.15, there is a gap between the estimated and measured lifetime which indicates that there are non-metallic traps present. The improved radial resolution shows that the lifetime changes a lot in the radial direction further out than $R = 4$cm. Corresponding to the previous results, the trap concentration seem to decrease with increasing length, as “Est.-” and “Meas. 2” has a larger gap than “Est.-” and “Meas. 4.”

The defect distribution on the bottom of the Cu decorated sample in figure 3.1.13 was uncertain, as the lifetime measured here seemed unexpectedly homogenous. The reason may be due to an absence of defects, a homogeneity of defects or an insufficient decoration process. If the Cu decoration *was* successful, the reason for the high lifetime here compared to farther up may be due to the traps being independent of the defects here. Another possibility is that there is only one type of defects here.

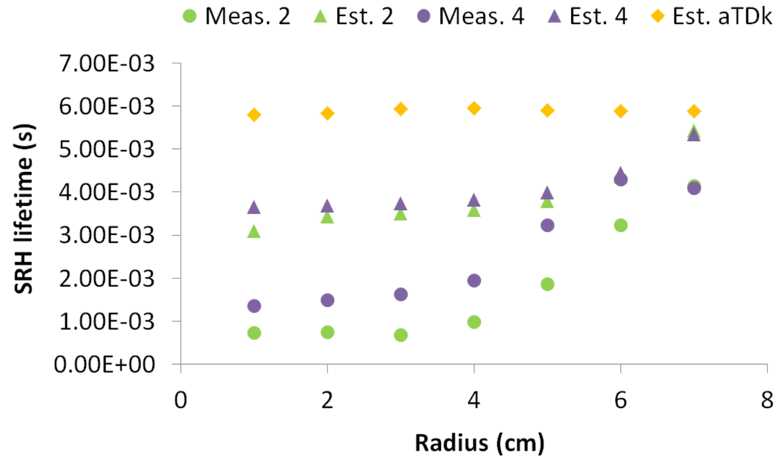

Figure 4.5.16: The radial change in lifetime for the first 20cm. The triangles symbolize the estimated radial change in lifetime, assumed that iron is the trap contributor, before thermal donor killing. The yellow diamonds are the estimated lifetime after thermal donor killing. The measured lifetime before thermal donor killing was plotted as circles. The label numbers illustrate how far from the shoulder the measurements were taken. As the coil was 4 cm long, "Meas. 2" was taken 5 − 9cm, and "Meas. 4" was taken at 13 − 17 cm. "Est. 2" and "Meas. 2" are from the same coordinates on the sample, and the same is true for "Est. 4" and "Meas. 4".

Meas. 4 on figure 4.5.16, which should be representative for the high lifetime area at the bottom of the Cu decorated sample in figure 3.1.13, indicate that the trap density is larger in the center than at the edge of the ingot. This deviates from the homogenous pattern in the same area in figure 3.1.13. This inconsistency indicates that the high lifetime at the bottom of the Cu-decorated sample is due to unsuccessful Cu-decoration.

In section 4.4, it was argued that the reduced lifetime between 1 and 5 cm on the outside of the ingot was either due to thermal donors or traps. The most likely

reason is non-metallic traps rather than thermal donors, as these traps seem to have a higher effect on the lifetime contrast. Metallic traps are unlikely, due to the estimated metallic distribution being much higher than the measured. It is also arguable that effect is a heightening of the lifetime at 5 cm instead of a lowering at 1cm, as 5cm is within the bubble, which has a relatively high lifetime. It is likely that the PCD has penetrated the sample deeper than the thickness of the red zone at 1cm on figure 3.4.2, hence reducing the average measured bulk lifetime here.

4.5.3.2 The cause of non-metallic traps

Non-metallic traps in the cross section may be caused by oxygen precipitates or lattice defects, which changes in accordance with the growth conditions, V/G. Oxygen can also introduce traps (O-donors at 0.07eV above the VB (11), and 0.17 under the CB when interstitial oxygen is trapped by a vacancy (13)), and it is plausible that the large concentrations of oxygen found in the center of the top part contributes to the lowering of the lifetime. In Yu Hu et. al. (2012) (45), the trap density was found to have "a positive correlation with concentration of interstitial oxygen and especially TDs in as-grown ingot".

As mentioned in section 1.1, the most effective traps are close to the center of the band gap. On the other hand, the measured concentration of oxygen in the center is high. Based on this, oxygen as interstitial or TD is a plausible cause of the non-metallic traps. On the other hand, since the traps are changing more rapidly than the thermal donor concentration, traps related to thermal donors are not regarded as likely to cause a lifetime degradation to this extent. The oxygen concentration also changes little with length during the first 18cm, indicating that potential interstitial oxygen traps are of less significance too. The CDI in figure 3.4.2 argues that the non-metallic traps are in fact defect related, as the lifetime pattern seem to follow the defect pattern shown in figure 3.1.1.

Figure 4.5.17, taken from Yu Hu et. al (2011) (45) is another Cz n-type ingot, named CZ1. Here, no significant difference in lifetime between the interstitial and the vacancy rich areas was found. There is also a low lifetime area in the top center part of the ingot that is thought to be due to thermal donors (38; 44). The increasing lifetime in figure 4.5.18 is an indication of this, as the distribution of phosphorous should give a *decreasing* trend in the lifetime. There is a possibility that a very high concentration of thermal donors would overshadow the interstitial part where, based on the observations in CZ2, a higher lifetime would be expected.

The resistivity measurements, however, indicate that the both the dopant concentration and the thermal donor concentration in CZ1 was similar to that in

CZ2 (44). Thermal donors is therefore believed to be an unlikely reason for the low contrast between the different defect dominated areas. Consequently, it seems that in CZ2 there are traps associated with the vacancy rich area that are not found in the vacancy rich area in CZ1.

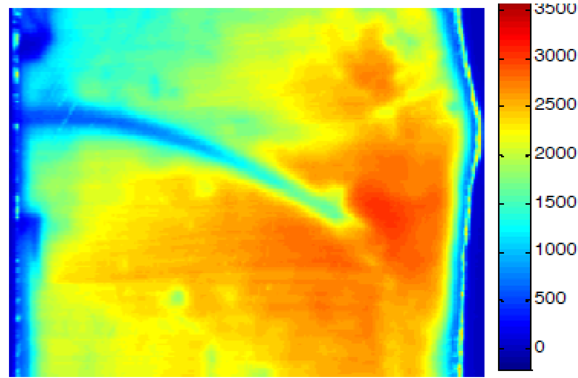

Figure 4.5.17: The CDI of CZ1 (45). No difference between the interstitial and vacancy rich regions appeared. Thermal donors are believed to cause the low lifetime at the center (left hand side). The band in the middle of the sample was believed to be a P-band.

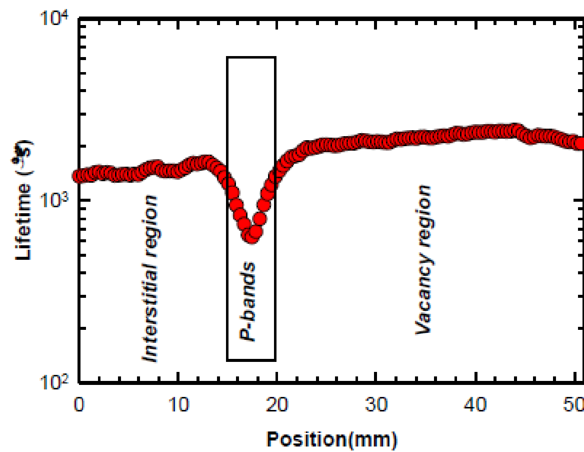

Figure 4.5.18: Measured 1.5cm away from the center of the ingot (45). Here, the thermal donor concentration is expected to be high. The lifetime increases slowly, as expected from a donor controlled lifetime.

According to J.M. Hwang et. al, the effective lifetime as a function oxygen particles (OPs) can be described by equation 4.27(46), when neglecting the effect of surface recombination, as the sample thickness was> 1cm for the lifetime measurements. τ_{op} can be described by equation 4.28. τ_{op}= OP lifetime (s), N_{op} = OP density (cm^{-3}), s = surface recombination of particle (cm/s), r_0 = radius (Å).

$$\frac{1}{\tau_{eff}} = \frac{1}{\tau_{op}} + \frac{1}{\tau_b} \tag{4.27}$$

$$\tau_{op} \approx (4\pi N_{op} s r_0^2)^{-1} \tag{4.28}$$

An increase in both r and N_{op} can lead to a reduced τ_{eff}. In figure 3.4.2, the lifetime in the vacancy rich area may be lowered due to such small, densely distributed oxygen particle defects typically found in the H- and L-bands. This band may also be recognized after Cu decoration in figure 3.1.11, which indicates that the density of defects very high here. The proposed hypothesis of a H- or L-band may explain the high lifetime degradation here.

The reason for the different effect of defect types in CZ1 and CZ2 may thus be explained by the absence of a broad L- or H- band in CZ1, as self interstitials and voids do not seem create contrasts in the lifetimes measurements themselves. The presence of oxygen, more importantly the formation of oxygen-void particles such as those found in H- and L-bands, is thus a plausible explanation to the reduction in lifetime in CZ2. This may emphasize the importance of the V/G ratio on lifetime degradation. Investigations of the low lifetime band in a SEM should be done to confirm the presence of oxygen particles.

It is however uncertain if such oxygen particle bands alone can be responsible for all the non-metallic traps, as the non-metallic traps found at the outside of the ingot does not seem to be related to oxygen particles. A possible explanation is that even though there seemed to be no difference between vacancy and self interstitial rich areas, these defects still may generate traps, only of similar total efficiency. It is likely that the non-metallic traps on the outside of the ingot is defect related, and thus dependent on the V/G ratio. The trap effect of different defects should thus be further investigated.

4.6 Contributions to lifetime degradation in CZ2

Possible lifetime reducing agents in the CZ2 ingot can be categorized into:

1. Donor effects
   (a) Dopants
   (b) Thermal donors
2. Traps
   (a) Metallic traps
   (b) Non-metallic traps

To sum up, there seems to be four main plausible contributions to the lifetime degradation in the ingot, given equation 4.26, where $X = X_1 + X_2 + X_3$:

- C_s lowers the lifetime from Auger to SRH lifetime due to *metallic traps*
- X_1 lowers the lifetime from the estimated to the outer measured lifetime, and is due to *non-metallic traps*
- X_2 is the contribution from the *thermal donors*, which were found in the center of the ingot
- X_3 reduces the lifetime from the thermal donor level to the measured level in the center of the ingot, due to *additional non-metallic traps* that seem to be caused by oxygen particles in an H- or L-band

N_T can now be described according to equation 4.29, where X_2, $X_3 = 0$ on the outside of the ingot. Figure 4.6.1 and 4.6.2 shows concept sketches of the different contributions to the SRH lifetime in a lengthwise and radial manner, respectively. The proportions of the different contributions are not accurate, and are merely meant to illustrate how they may influence the lifetime.

$$N_T = C_s + X_1 + X_2 + X_3 \tag{4.29}$$

The investigation indicates that the presence of non-metallic traps seems relatively certain, as these traps were not Scheil distributed. The concentration of non-metallic traps was also found to be larger in the center of the ingot than at the edge. The amount of C_s, X_1, X_2 and X_3 in the total N_T is difficult to calculate without a certain knowledge of the concentration of the different

contaminants in the ingot. The graphs in figure 4.5.14, 4.5.15 and 4.5.16 merely show the *maximum* possible lifetime reduction due to iron.

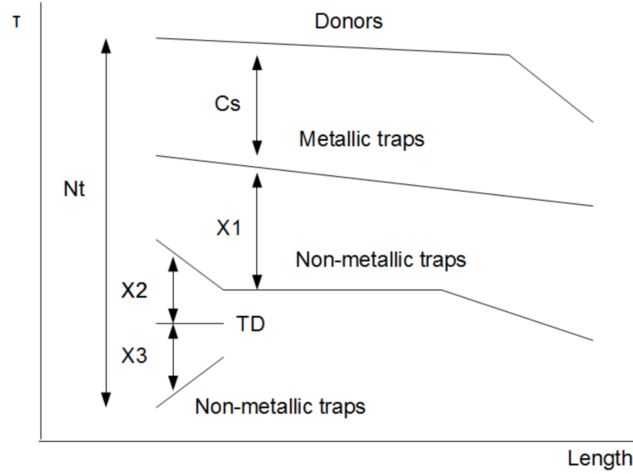

Figure 4.6.1: $C_s$is the contribution from metallic traps, X_1 is the contribution of non-metallic traps that contributes to lower the lifetime to the level measured on the outside of the ingot. X_2 and X_3 is the contribution of the thermal donors and (possibly) defect related non-metallic traps found only in the cross section. N_T is the total trap density. $X_3$is believed to be the cause of the lifetime reduction in the center of the ingot compared to the outside of the ingot, and seems to be caused by oxygen particles. The proportions of the different contributions are not accurate, and are merely meant to illustrate how they may influence the lifetime.

Figure 4.6.3 shows the estimated SRH lifetime with only iron traps (including height correction with $\Delta\tau_{SRH}$), compared with the measured lifetime and estimated Auger lifetime. In this example, the iron traps seem to be the main cause of the lifetime reduction. Metallic traps are Scheil distributed, making the shape of the curve relatively predictable. The height of the curve, on the other hand, cannot be decided by the results in this thesis, as iron was merely an example. A reduction in the assumed metal density would heighten the metallic trap curve in figure 4.6.3 towards the Auger lifetime.

The amount of non-metallic traps compared to metallic traps is thus also uncertain, as a heightening of the metallic trap curve would lead to a compensation of lowering the non-metallic trap curve, as the trap level in CZ2 is constant for each position. There is a relatively high chance that the concentration of non-metallic traps is higher, and that other metallic traps exist in the ingot besides iron. Although the concentration of all metals in the ingot can theoretically be equal to zero, this requires an extremely pure feedstock, which is highly unlikely.

The size of X_1 is unstable, which may be due to the V/G rate, assuming that it is defect dependent.

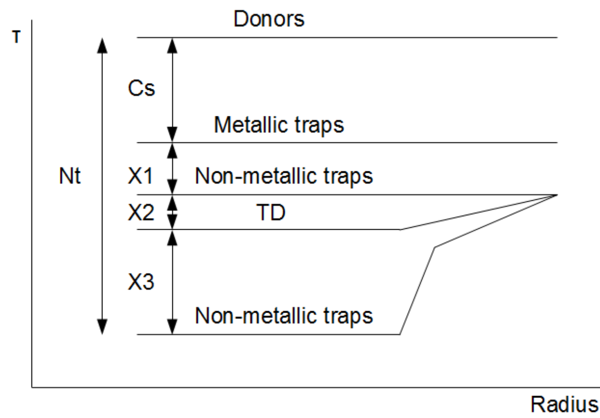

Figure 4.6.2: The symbols are the same as in figure 4.6.1. The sketch shows the lifetime lowering agents in the cross section of the top part of the ingot (above 10cm) from a radial perspective. Though there is a contribution from thermal donors in the center of the ingot, non-metallic traps seem to be more important for the degradation of the lifetime here.

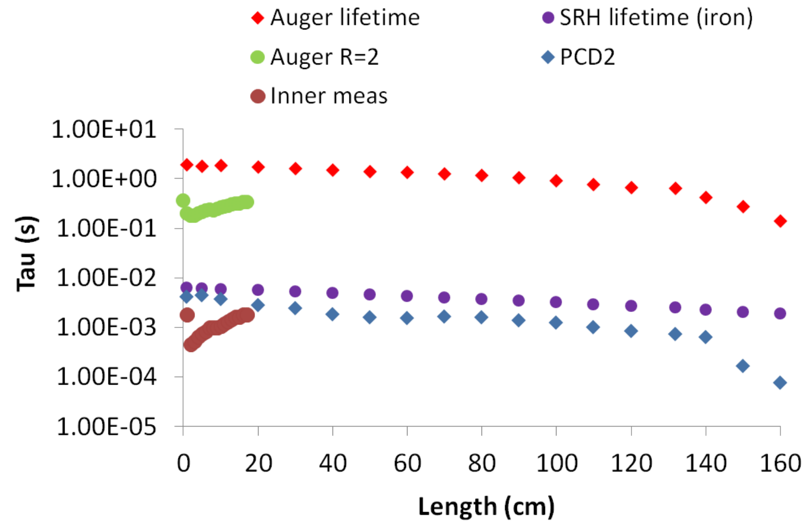

Figure 4.6.3: Estimated SRH lifetime (cause of traps assumed to be iron), estimated Auger lifetime (both with and without thermal donors), and measured lifetime (both on the outside of the ingot and in the center).

The traps in CZ2 generally seem to have a much larger influence on the lifetime than thermal donors, due to the large gap between Auger and SRH lifetime being greater than the gap between Auger and/or SRH lifetime and thermal donors. To improve the lifetime, purification of the feedstock is necessary if metallic contaminants are the main source of the traps. Control of the oxygen concentration and the V/G ratio may also be important and logical approaches for removing non-metallic traps.

4.7 Contrast in lifetime measurements

A benefit of metallic traps is that the Scheil distribution (as long as it is stable, as in the top parts of an ingot) makes the lifetime more or less “transparent” to other lifetime reducing effects, which may become visible as contrasts in a CDI due to rapid changes in N_T. Using a PCD, this seems to show up as steep curves. In CZ1 from Yu Hu et. al. (2011) (45), the both the P-band and the thermal donors seemed to give a contrast on the CDI in figure 4.5.17, as the change in thermal donor concentration and the P-band presumable was the steepest of the lifetime reducing agents.

In CZ1, shown in figure 3.4.2, the lifetime degradation agent with the most rapid change seemed to be oxygen particles in a H- or L-band. Even though thermal donors were present, the contrast from this seemingly was not enough to “overshadow” the contrast from the plausible oxygen particle traps, even though both the lengthwise and radial change was rapid compared to possible metallic traps and dopants. Possible explanations for the transparent nature of the thermal donors in CZ2 may be:

1. The assumed oxygen particle related traps in the center are much more efficient than the contribution from the thermal donors
2. The efficiency of the defect related traps and the thermal donors are similar, thus the concentration defect related traps should be larger. This would again increase the total trap density, X, pushing all the estimated lifetimes closer to the Auger lifetime. In practice, this would mean that the metallic concentration is lower than assumed in figure 4.5.11, even after corrections with $\Delta C_{sr(Fe,Y)}$.
3. A combination of 1. and 2.

It is thus important to remember that even though the contrast (or the most rapid change) is what appears on the measurements, the cause of this contrast is not necessarily the main cause of the lifetime reduction, as the influence of the transparent metallic traps may have a greater influence on the lifetime than the defect related traps.

Conclusion

The resistivity measurements revealed thermal donors in the cross section of the ingot during the first 18cm. Measuring the resistivity before and after TD-killing, and replacing N_D with $N_D + 2[TD]$ in the case with thermal donors, works for both equation 1.6 and 1.10, and can be used to find [TD] if N_D is known. The standard deviation of the resistivity measurements done on the outside of the ingot was calculated to $s = 0.183$. Deviations between PCD and FPP results was believed to be due to poor contact with the material when using the PCD. However, this was believed to not have an influence the lifetime measurements in transient mode.

The lifetime is expected to increase with increasing length of the ingot, as the dopant is Scheil distributed. The lifetime measurements from the outside of the ingot were found to follow this expected behavior, with the exception of the first 5cm. The increase in lifetime here was believed to be due to the penetration depth of the PCD. A low lifetime area was found in the center of the ingot, which was only separated from the edge by a perfect crystal/self interstitial band of about 1.5cm, and which was found to be thicker at $Y = 5$cm than at $Y = 1$cm.

In the center of the ingot, non-metallic traps related to oxygen precipitates, producing an H- or L-band, were believed to cause the rapid unexpected increase in the measured lifetime in the first 18cm. Lifetime estimations indicated that SRH recombination was the dominant recombination mechanism in the entire ingot, and the traps seemed to lower the lifetime considerably much more than the thermal donors.

The cause of the non-metallic traps found on the outside of the ingot, which seemed to be unrelated to oxygen particles, is unknown. There is a possibility that they may be related to defects, and further investigations should be done to confirm or dis-confirm this hypothesis. A structure loss in the tail also seemed to heighten the trap density. Other sources of traps were found in interstitial oxygen and thermal donors, but the influence of these were believed to be modest, and not present on the outside of the ingot.

Metallic traps were assumed to be present as well. The concentration and type of metals present were unknown, however. How much of the trapping that is due to metallic traps compared to the non-metallic traps is uncertain, and contaminant investigations should be done to get a better overview of this. If metallic traps were found to be the main cause, purification methods should be improved. If non-metallic traps are dominant, further investigations on the effect of the V/G ratio should be done.

Using a CDI mapping of the lifetime, the contrast in the image seemed to be due to the contribution that changes the most rapidly. Scheil distributed trap elements, such as certain metal impurities, were believed to be transparent high up in the ingot due to the even metal distribution here. It is likely that other, more evenly distributed, and hence more transparent traps, were more influential to the reduction of the lifetime that traps that causes contrast.

Further work

- Investigation on the concentration of various metallic contaminants, and estimate SRH lifetime based on the metal trap concentration. This may give an indication of whether the traps are caused by metallic contaminants or not.
- Investigate the ingot between 18-30cm to investigate the thermal donor distribution further down in the ingot.
- Cu decoration on the area 10-30cm to investigate the continuation of the defect pattern and confirm or dis-confirm the suspicion of insufficient Cu decoration at the bottom of sample 4.
- Compare perfect crystalline Si with defect dense Si to investigate the trap effect of self interstitials and vacancies free from oxygen particles.
- Investigate the presence of oxygen particles in the low lifetime area during the first 18cm in a SEM.
- Investigate the reason for the lack of increase in O_i concentration after thermal donor killing.
- CDI of the cross section between 8-30cm to investigate the defect influence on the lifetime further down in the ingot.
- Investigate how much the individual defect types influence the lifetime.
- Investigate the reason for the "inverse" symmetry of defects in the two Cu decorated samples, as well as the deviation inside the "bubble".

Bibliography

[1] E.A Alsema and E Nieuwlaar. Energy viability of photovoltaic systems. *Energy Policy*, 28(14):999 – 1010, 2000. <ce:title>The viability of solar photovoltaics</ce:title>.

[2] Environmental impacts of crystalline silicon photovoltaic module production. *Presented at 13th CIRP Intern. Conf. on Life Cycle Engineering, Leuven, 31 May- 2 June 2006*, 2006.

[3] European Photovoltaic Industry Association. solar photovoltaics competing in the energy sector - on the road to competitiveness. In *Proceedings from the 26th European PVSEC, Hamburg, Germany*, 2011.

[4] Solar Winds USA. Solar panel. `http://www.solarwindsusa.com/magento/solar-panels.html`, 2012.

[5] Eivind Ovrelid. Personal communication, 2012.

[6] J E Cotter, J H Guo, P J Cousins, M D Abbott, F W Chen, and K C Fisher. P-type versus n-type silicon wafers: Prospects for high-efficiency commercial silicon solar cells. *IEEE Transactions on Electron Devices*, 53(8):1893–1901, 2006.

[7] Bhatt Devesh Prasad Joshi, Dinesh Prasad. Theory of grain boundary recombination and carrier transport in polycrystalline silicon under optical illumination. *IEEE Transactions on Electron Devices*, 37(1):237–249, 1990. cited By (since 1996) 15.

[8] Martin A. Green, Keith Emery, Yoshihiro Hishikawa, Wilhelm Warta, and Ewan D. Dunlop. Solar cell efficiency tables (version 39). *Progress in Photovoltaics: Research and Applications*, 20(1):12–20, 2012.

[9] Veikko Lindroos. *Handbook of silicon based MEMS: materials and technologies*. Elsevier Science [distributor], Norwich, N.Y.

[10] G. Coletti. Sensitivity of state-of-the-art and high efficiency crystalline silicon solar cells to metal impurities. *Progress in Photovoltaics: Research and Applications*, 2012. cited By (since 1996) 0; Article in Press.

[11] Dieter K. Schroder. *Semiconductor material and device characterization.* IEEE Press, Hoboken, N.J., 2006. "Wiley-Interscience." 3rd ed.

[12] Martin A. Green. *Solar cells: operating principles, technology and system applications.* University of New South Wales, Kensington, 1992. Opptrykk. Opprinnelig utg.: Englewood Cliffs, N.J. : Prentice Hall, c1982.

[13] W. Schroter and Peter Haasen. *Electronic structure and properties of semiconductors.* Materials science and technology: a comprehensive treatment. Wiley-VCH, Weinheim, 2005. Vol. 4/5.

[14] Geerligs L.J. Macdonald, D. Recombination activity of interstitial iron and other transition metal point defects in p- and n-type crystalline silicon. *Applied Physics Letters*, 85(18):4061–4063, 2004. cited By (since 1996) 64.

[15] J.B. Little G.K. Teal. Growth of germanium single crystals. *Phys. Rev. 78*, 1950.

[16] E. Buehler G.K. Teal. Growth of silicon single crystals and single crystal silicon pn junctions. 1952.

[17] H.R. Huff. From the lab to the fab, transistors to integrated circuits, in: C. claeys, f. gonzalez, r. singh, j. murota, p. fazan (eds.), ulsi process integration iii. page 15, 2003.

[18] Per K. Kofstad. Silisium. `snl.no/silisium`, 2011.

[19] Silfex. custom silicon ingots and blanks. `http://www.silfex.com/products_2_0.html`, 2012.

[20] Gianluca Coletti. Impurities in silicon and their impact on solar cell performance. Utrecht University, 2011.

[21] E. Scheil. Bemerkungen zur schichtkristallbildung. *Zeitschrift fur Metallkunde 34*, pages 70–72, 1942.

[22] Gianluca Coletti, Paula C. P. Bronsveld, Giso Hahn, Wilhelm Warta, Daniel Macdonald, Bruno Ceccaroli, Karsten Wambach, Nam Le Quang, and Juan M. Fernandez. Impact of metal contamination in silicon solar cells. *Advanced Functional Materials*, 21(5):879–890, 2011.

[23] Semiconductor Equipment and Materials International. Semi mf723-0307 - practice for conversion between resistivity and dopant or carrier density for boron-doped, phosphorus-doped, and arsenic-doped silicon. Technical report, SEMI.

[24] William C. O'Mara, Robert B. Herring, and Lee P. Hunt. *Handbook of semiconductor silicon technology.* Crest Publ. House, New Delhi, 2005.

[25] Pensl G. Zulehner W. Newman R.C. McQuaid S.A. Gotz, W. Thermal donor formation and annihilation at temperatures above 500 â°c in czochralski-grown si. *Journal of Applied Physics*, 84(7):3561–3568, 1998. cited By (since 1996) 13.

[26] Dubois S. Enjalbert N. Lemiti M. Veirman, J. A fast and easily implemented method for interstitial oxygen concentration mapping through the activation of thermal donors in silicon. volume 8, pages 41–46, 2011. cited By (since 1996) 0.

[27] Hauser John R. Roulston David J. Arora, Narain D. Electron and hole mobilities in silicon as a function of concentration and temperature. *IEEE Transactions on Electron Devices*, ED-29(2):292–295, 1982. cited By (since 1996) 230.

[28] W. Shockley and W. T. Read. Statistics of the recombinations of holes and electrons. *Phys. Rev.*, 87:835–842, Sep 1952.

[29] V.V. Voronkov. Grown-in defects in silicon produced by agglomeration of vacancies and self-interstitials. *Journal of Crystal Growth*, 310(7-9):1307–1314, 2008. cited By (since 1996) 4.

[30] Stein Bekkevold. Gradient - varmeteknikk. `http://snl.no/gradient/varmeteknikk`, 2011.

[31] E. Ovrelid L. Arnberg Yu Hu, M. Juel. Comparison of different techniques for characterization of defects in n-type cz silicon. In *Proceedings from the 26th European PVSEC, Hamburg, Germany*, 2011.

[32] Ross Boyle. Ft-ir measurement of interstitial oxygen and substitutional carbon in silicon wafers. `http://www.thermo.com`, 2012.

[33] Haldor Topsoe. *Geometric factors in four point probe resistivity measurements*. 1966.

[34] Hunter W.g. Hunter J.S. Box, G.E.P. *Statistics for Experiments*. John Wiley and Sons, 1978.

[35] N.C. Barford. *Experimental Measurements: Precision, Error and Truth*. John Wiley and Sons, 1985.

[36] J. Isenberg, S. Riepe, S.W. Glunz, and W. Warta. Carrier density imaging (cdi): a spatially resolved lifetime measurement suitable for in-line process-control. In *Photovoltaic Specialists Conference, 2002. Conference Record of the Twenty-Ninth IEEE*, pages 266 – 269, may 2002.

[37] Vivian Sporstoel Koien. Characterization of defects in n-type cz-si. Project Thesis, 2011.

[38] Yu Hu. Personal communication, December 2011.

[39] H Nagel, C Berge, and AG Aberle. Generalized analysis of quasi-steady-state and quasi-transient measurements of carrier lifetimes in semiconductors. *JOURNAL OF APPLIED PHYSICS*, 86(11):6218–6221, DEC 1 1999.

[40] W. Wijaranakula. Formation kinetics of oxygen thermal donors in silicon. *Applied Physics Letters*, 59(13):1608 –1610, sep 1991.

[41] G. H. Aylward and T. J. V. Findlay. *Si chemical data*. Wiley, Milton, 2008. 6th ed.

[42] Adrienne Blum. Personal communications. Bct-300, Tech Support, Sinton Instruments.

[43] M.A. Green. Intrinsic concentration, effective densities of states, and effective mass in silicon. *Journal of Applied Physics*, 67(6):2944–2954, 1990. cited By (since 1996) 149.

[44] Mari Juel. Personal communication, June 2012.

[45] Oyvind Nielsen Eivind Johannes Ovrelid Lars Arnberg Yu Hu, Hendrik Schon. Investigating minority carrier trapping in n-type cz silicon by transient photoconductance measurements. *Journal of Applied Physics*, 111(5):053101 –053101–6, mar 2012.

[46] J. M. Hwang and D. K. Schroder. Recombination properties of oxygen-precipitated silicon. *Journal of Applied Physics*, 59(7):2476 –2487, apr 1986.

Appendices

Appendix 1

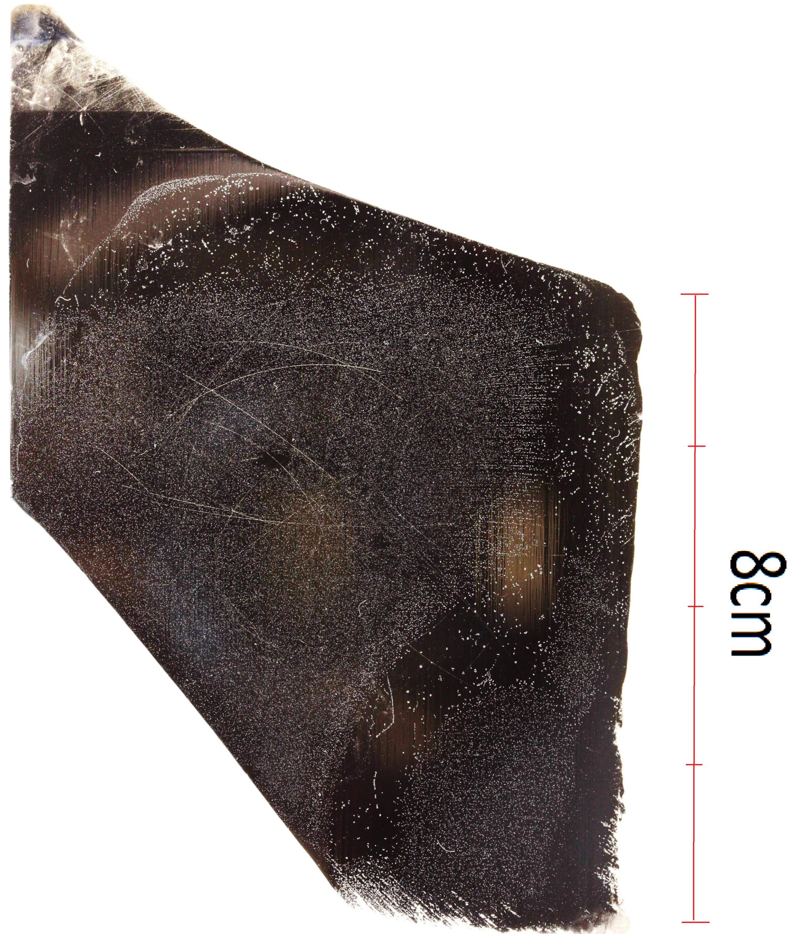

Figure 4.7.1: Sample 3a

Appendix 2

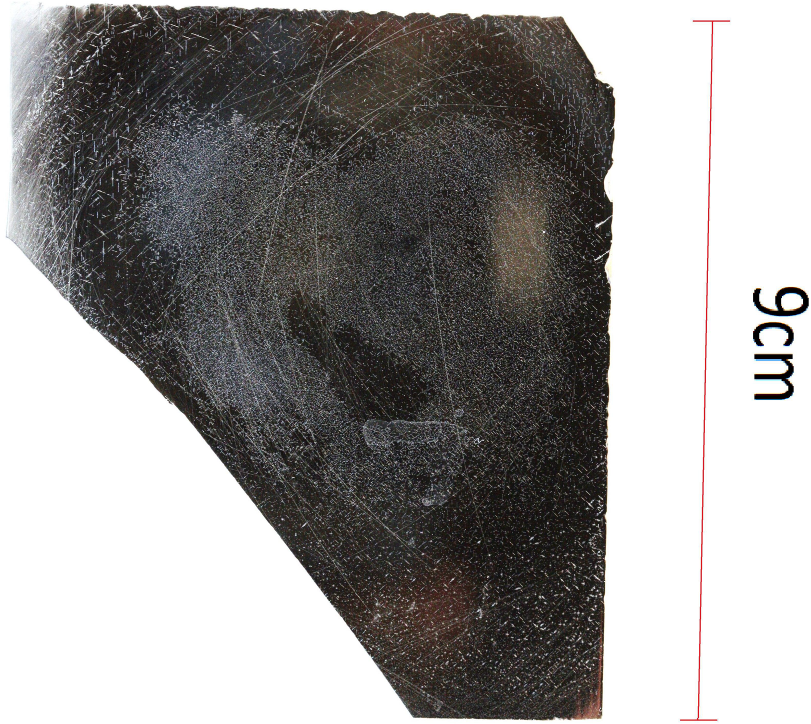

Figure 4.7.2: Sample 3b

Appendix 3

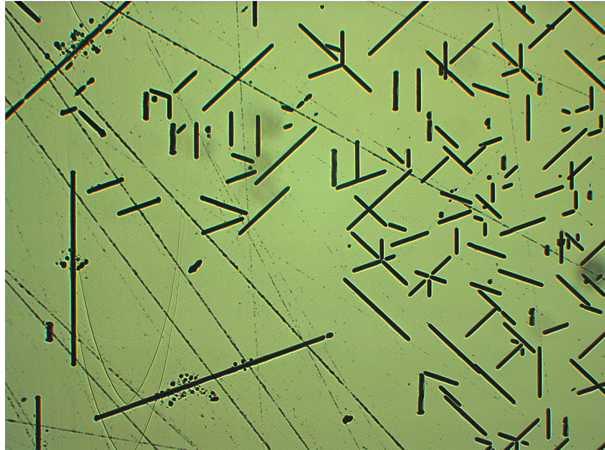

Figure 4.7.3: Sample 3b, $Y \approx 10$, $R \approx 1$. The line defects are actually surface defects due to scratching.

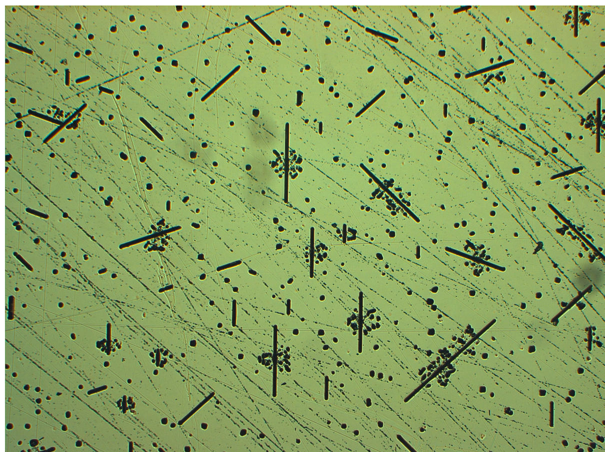

Figure 4.7.4: Sample 3b, $Y \approx 17$,$R \approx 1$. The sample is corrupted bu surface scratch defects that has nothing to do with the V/G rate.

Appendix 4

Figure 4.7.5: Band surrounding the “bubble” on sample 4.

Appendix 5

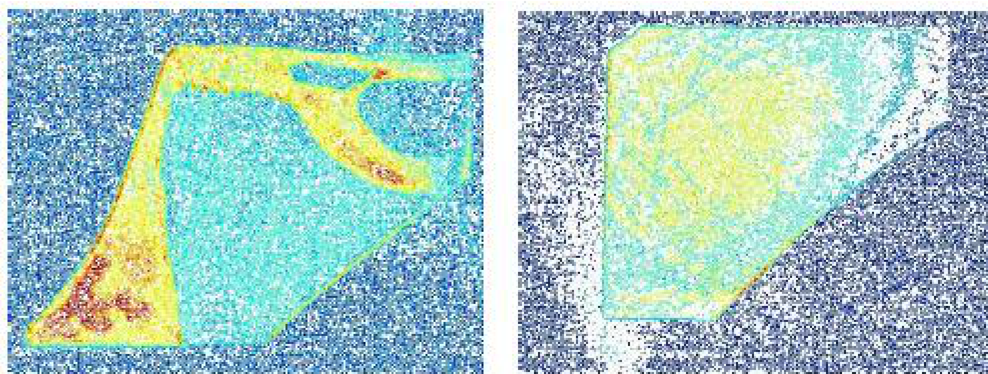

Figure 4.7.6: Sample 3a (left) and 3b (right). The Cu decoration of 3b was unsuccessful.